

# Skin-Friction and Forced Convection from Rough and Smooth Plates

Aubrey G. Jaffer  
e-mail: agj@alum.mit.edu

## Abstract

Since the 1930s, theories for skin-friction drag from plates with rough surfaces have been based on analogy to turbulent flow within pipes having rough interiors. Failure of this analogy at low Reynolds number ( $Re$ ) flow rates has frustrated attempts to create a comprehensive theory.

By introducing the concept of a self-similar roughness, the present work derives formulas for a plate's skin-friction drag coefficient and turbulent forced convection given its root-mean-squared height-of-roughness and isotropic spatial period. These formulas are in agreement with measurements from Pimenta, Moffat, and Kays (1975), Bergstrom, Akinlade, and Tachie (2005), and experiments conducted by the present author.

The present work also derives a formula for skin-friction coefficient of a smooth plate; this formula is in very close agreement with measurements from Smith and Walker (1959) and Spalding and Chi (1964) spanning 5 decades of  $Re$ . Its new formula for turbulent forced convection is in agreement with Lienhard (2020), while expanding the range to all fluid Prandtl numbers.

This research did not receive any specific grant from funding agencies in the public, commercial, or not-for-profit sectors.

## Table of contents

1. <i>Introduction</i> .....	2
2. <i>Roughness metrics</i> .....	3
3. <i>Sand-roughness</i> .....	4
4. <i>Prior work formulas</i> .....	5
5. <i>Rough turbulence</i> .....	6
6. <i>Profile roughness</i> .....	6
7. <i>Self-similar ramp permutations</i> .....	7
8. <i>Roughness travel</i> .....	8
9. <i>Skin-friction from a rough plate</i> .....	9
10. <i>Skin-friction from a smooth plate</i> .....	9
11. <i>Spectral roughness</i> .....	11
12. <i>Periodic roughness</i> .....	12
13. <i>Onset of rough turbulence</i> .....	13
14. <i>Flat-peaked roughness</i> .....	14
15. <i>Bi-level roughness</i> .....	15
16. <i>Flow modes</i> .....	16
17. <i>Local skin-friction</i> .....	17
18. <i>Forced convection from a rough plate</i> .....	18
19. <i>Forced convection from a smooth plate</i> .....	18
20. <i>Periodic versus self-similar roughness</i> .....	22
21. <i>Fully rough regime</i> .....	22
22. <i>Transitional rough regime</i> .....	23
23. <i>Sandpaper</i> .....	25
24. <i>Woven wire mesh</i> .....	26
25. <i>Perforated sheet</i> .....	27
26. <i>Convection measurements</i> .....	28
27. <i>Discussion</i> .....	29
28. <i>Conclusions</i> .....	30
29. <i>Nomenclature</i> .....	31
30. <i>References</i> .....	32
31. <i>Appendix: convection measurement apparatus and methodology</i> .....	33

## 1. Introduction

Skin-friction drag is the pressure opposing flow due to viscous dissipation of turbulence generated by that flow along a surface. Skin-friction is important to the fluid dynamics of vehicles and turbines. The related phenomenon of forced convection has application to modeling weather and the thermal behavior of buildings.

The present work uses the terms “resistance”, “skin-friction”, “drag”, and “skin-friction drag” interchangeably; also “rough” and “fully rough”; also “smooth” and “hydraulically smooth”; also “turbulence” and “turbulent flow”; also “free-stream” and “bulk flow”.

In 1934, Prandtl and Schlichting [1] inferred a relation for skin-friction resistance for rough plates from their analysis of Nikuradse’s [2] measurements of sand glued inside pipes (“sand-roughness”). At the conclusion of the paper they write:

“The resistance law just derived for rough plates has chiefly validity for a very specific type of roughness, namely a smooth surface to which sand grains have been densely attached and where the Nikuradse pipe results have been taken as the basis. . .

A single roughness parameter (the relative roughness) will in all likelihood no longer answer the purpose in continued investigations of the roughness problem.”

In 1936 Schlichting [3] investigated the velocity field and friction coefficients of water flowing through a closed rectangular channel having one wall replaced in turn by a series of 23 plates, each having an array of identical protrusions attached: spheres, spherical caps (bumps), cones, short angle irons, long angle irons (spanning the plate), and Hamburg sand. The placement of protrusions on nearly all of the plates was a hexagonal array stretched 15% in the direction of flow.

There was significant pressure drop between the inflow and outflow of the channel, so it wasn’t an example of the isobaric (no pressure drop) flow which occurs along external plates. The similarity of closed channel flow to pipe flow is well known, but doesn’t support or refute treating pipes and plates analogously.

Hama [4] describes three challenges to the pipe-plate analogy:

“Now there is no obvious reason why pipe flow and boundary-layer flow should be identical or even similar. First, a pressure gradient is essential for flow through a pipe but not along a plate. Second, pipe flow is confined and perforce uniform, while flow along a plate develops semi-freely and bears no such a priori guarantee of displaying similar velocity profiles at successive sections. Finally, the diameter and roughness size are the only geometrical dimensions of established flow in pipes, whereas at least three linear quantities are necessary to characterize the boundary-layer.”

Flow at the plate surface has zero velocity. The “boundary-layer” is flow near the surface which has velocity different from the bulk flow velocity  $u$ . Hama reserves the term boundary-layer for flow along plates.

Hama attempts to confirm the pipe-plate analogy with measurements of wire screens affixed to smooth plates, but concludes that it is confirmed only in the fully rough regime (defined below).

Roughness in prior works [1, 2, 3, 4, 5, 6, 7, 8, 9] is reported in sand-roughness  $k_S$ , the height of “coarse and tightly placed roughness elements such as for example coarse sand grains glued on the surface” [7].

A machined analogue to sand-roughness, the plate tested by Pimenta, Moffat, and Kays [5] was composed of 11 layers of densely packed metal balls 1.27 mm in diameter “arranged such that the surface has a regular array of hemispherical roughness elements.” The reported sand-roughness of the plate was  $k_S = 0.794$  mm. Pimenta et al write that, while the agreement of their data with the Prandtl-Schlichting plate model is “rather good” in the fully rough regime, their apparatus doesn’t have the same behavior as “Nikuradse’s sand-grain pipe flows in the transition region”.

Taking the wake component of the velocity profile into account, Mills and Hang [6] created a formula improving the match to Pimenta et al data in the rough regime, but was silent about the other flow regimes.

The theory for flow within pipes and channels distinguishes three turbulent flow regimes: smooth, rough, and transitional. Smooth pipe flow encounters viscous resistance which varies inversely with the ratio of fluid velocity to viscosity. Rough pipe flow encounters resistance which varies with the height-of-roughness while the effect of viscosity is negligible. The transitional regime describes the range of Reynolds number ( $Re$ ) flow rates where both viscosity and roughness affect the resistance (Colebrook [10]).

In pipes, the resistance of rough flow is never less than the resistance of smooth flow at the same (diameter, viscosity and)  $Re$  flow rate. An unstated tenet of the pipe-plate analogy is that this relation

holds for external plates. Pimenta et al finding that pipe and plate behavior differed in the transition region is an understatement. Their data shows (in present work Figures 21 and 22) that rough regime resistance can be less than smooth regime resistance. This should have invalidated the pipe-plate analogy. But, because of an extra factor of 2 in the Prandtl-Schlichting theory, this wasn't realized, and research continued based on the pipe-plate analogy. In a 2004 survey article, Jiménez [11] writes: "The theoretical arguments are sound, but the experimental evidence is inconclusive."

Tachie, Bergstrom, Balachandar, and Ramachandran [12] combine multiple studies to propose a correlation for skin-friction coefficient in terms of the momentum-thickness Reynolds number  $Re_\theta$ :

$$C_f = 4.13 \times 10^{-2} - 2.68 \times 10^{-2} \log_{10} Re_\theta + 6.528 \times 10^{-3} \log_{10}^2 Re_\theta - 5.54 \times 10^{-4} \log_{10}^3 Re_\theta \quad (1)$$

In terms of a roughness metric, formula (1) has no predictive value because  $Re_\theta$  must be computed from velocity field measurements along the surface in question.

Bergstrom, Akinlade, and Tachie [13], performing experiments with sandpapers, woven-wire meshes, and perforated sheets attached to flat plates, find that the local skin-friction coefficient  $c_f$  satisfies:

$$c_f^{1/2} = (0.360 \pm 0.025) \frac{\delta^*}{\delta} \quad (2)$$

where  $\delta^*$  is the displacement thickness and  $\delta$  is the (99% velocity) boundary-layer thickness. In terms of a roughness metric, formula (2) has no predictive value because both  $\delta^*$  and  $\delta$  must be computed from velocity field measurements along the surface in question. Fortunately, Bergstrom et al included free-stream velocity  $U_e$  in their tables, allowing their measurements to be compared with the present theory.

In the discussion appended to Hama [4], Dr. S. F. Hoerner points out:

"... there is hardly any physical or natural surface condition which is truly equal or similar to sand roughness. One conclusion from sand experiments has been the expectation that from then on every rough surface should have a constant terminal drag coefficient. As early as 1924, it has been demonstrated (by Hopf and Fromm in *Zeitschr. Angew. Math. Mech.*, 1923:329-339) that certain types of roughness do not show any constant coefficients."

The lack of generality of sand-roughness as a metric, the need for additional roughness parameters, non-constant terminal drag coefficients, and the unrealized promise of the pipe-plate analogy motivate a fresh theoretical analysis of isobaric flow along plate roughness based on a traceable roughness metric.

## 2. Roughness metrics

Two widely used traceable roughness metrics are root-mean-squared (RMS) and arithmetic-mean height-of-roughness. For an elevation function  $z(x, y)$  defined on area  $A$  with a convex perimeter, its mean elevation  $\bar{z}$  and RMS height-of-roughness  $\varepsilon$  are:

$$\bar{z} = \int_A z \, dA / \int_A dA \quad \varepsilon = \sqrt{\int_A |z - \bar{z}|^2 \, dA / \int_A dA} \quad (3)$$

Arithmetic-mean height-of-roughness is also defined using mean elevation  $\bar{z}$ :

$$\int_A |z - \bar{z}| \, dA / \int_A dA \quad (4)$$

### 3. Sand-roughness

Modeling sand grains as diameter  $k_S$  spheres glued to a (horizontal) plate surface, with the area not covered by a sphere as glue of height  $g$ , the mean height of the cell of area  $A$  containing a sphere is:

$$\bar{z} = \int_0^{k_S/2} \frac{2\pi x}{A} \left[ \sqrt{\frac{k_S^2}{4} - x^2} + \frac{k_S}{2} \right] dx + \left[ A - \frac{\pi k_S^2}{4} \right] \frac{g}{A} = g + \frac{5\pi k_S^3}{24A} - \frac{\pi k_S^2 g}{4A} \quad (5)$$

Its RMS height-of-roughness is:

$$\varepsilon(k_S, g, A) = \sqrt{\int_0^{k_S/2} \frac{2\pi x}{A} \left| \sqrt{\frac{k_S^2}{4} - x^2} + \frac{k_S}{2} - \bar{z} \right|^2 dx + \left[ 1 - \frac{\pi k_S^2}{4A} \right] |g - \bar{z}|^2} \quad (6)$$

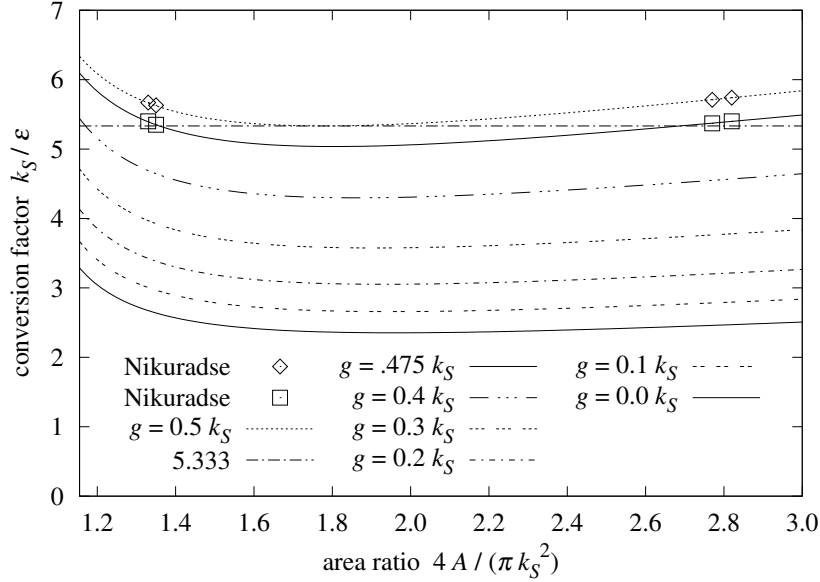


**Figure 1**  $k_S/\varepsilon$  versus cell area of sand-roughness

Figure 1 shows the  $\varepsilon$  to  $k_S$  conversion factor versus the cell to sphere area ratio at glue-levels from 0 to 50% of  $k_S$ .

$k_S$	grains/cm <sup>2</sup>	$k_S/\varepsilon$
.08 cm	150	5.67
.04 cm	590	5.63
.02 cm	1130	5.74
.01 cm	4600	5.71

**Table 1** Nikuradse's sand coatings

Table 1 shows the  $k_S$ , grain densities, and conversion factors for Nikuradse's [2] sand coatings, assuming  $g = 0.5 k_S$ . Even though the coatings had area ratios spanning a 2.1:1 range, their conversion factors match within 2%. These are the diamonds labeled "Nikuradse" in Figure 1.

Afzal, Seena, and Bushra [14] fit 5.333 for the RMS to sand-roughness conversion factor  $k_S/\varepsilon$  and 6.45 for arithmetic-mean to sand-roughness in pipes.  $k_S/\varepsilon = 5.333$  is a broad minimum for the  $g/k_S \approx 0.5$  curve in Figure 1, supporting the 50% glue level as a model for sand-roughness. The tightest  $k_S/\varepsilon$  spread ( $< 1\%$ ) for Nikuradse's coatings (squares in Figure 1) is centered on  $k_S/\varepsilon = 5.38$ , which occurs with  $g \approx 0.475 k_S$ .

The tightest spread achievable on Table 1 data with arithmetic-mean height-of-roughness is 24%. Thus, sand-roughness has a much stronger correlation with RMS height-of-roughness than with arithmetic-mean.

Flack, Schultz, Barros, and Kim [15] measured skin-friction from grit-blasted surfaces in a duct. They write "The root-mean-square roughness height is shown to be most strongly correlated with the equivalent sand-roughness height ( $k_S$ ) for the grit-blasted surfaces."

The plate tested by Pimenta et al [5] was composed of 11 layers of densely packed metal balls 1.27 mm in diameter. There was no glue level fitting the description of  $g$ . With the cell area shrunk to the sphere's shadow,  $\pi k_S^2/4$ , the RMS height-of-roughness of the top layer of 1.27 mm spheres is 0.150 mm, irrespective of  $g$ . Using the  $k_S \approx 0.794$  mm from Pimenta et al with the 5.333 conversion factor from Afzal et al yields  $k_S/5.333 \approx 0.149$  mm, which matches 0.150 mm within 1%.

#### 4. Prior work formulas

In *Boundary-layer theory* [7] Prandtl and Schlichting give formulas for fully rough local ( $c_f$ ) and plate average ( $\bar{c}_f$ ) skin-friction coefficient for a rough plate in terms of its sand-roughness  $k_S$  and the distance  $x$  along the plate in the direction of flow. The characteristic-length  $L$  is the length scale for the physical system; in these formulas,  $L$  is the plate length in the direction of flow.

$$c_f = \left( 2.87 + 1.58 \log_{10} \frac{x}{k_S} \right)^{-2.5} \quad x \leq L \quad (7)$$

$$\bar{c}_f = \left( 1.89 + 1.62 \log_{10} \frac{L}{k_S} \right)^{-2.5} \quad 10^2 < \frac{L}{k_S} < 10^6 \quad (8)$$

Mills and Hang [6] give a formula (9) which is more accurate than formula (7) on the local skin-friction measurements from Pimenta et al [5]. Their local ( $C_f$ ) and average ( $\bar{C}_f$ ) coefficient formulas are:

$$C_f = \left( 3.476 + 0.707 \ln \frac{x}{k_S} \right)^{-2.46} \quad x \leq L \quad (9)$$

$$\bar{C}_f = \left( 2.635 + 0.618 \ln \frac{L}{k_S} \right)^{-2.57} \quad 750 < \frac{L}{k_S} < 2750 \quad (10)$$

White [8] gives formula (11) for fully rough local skin-friction coefficient:

$$C_f = \left( 1.4 + 3.7 \log_{10} \frac{x}{k_S} \right)^{-2} \quad \frac{x}{k_S} > \frac{Re_x}{1000} \quad (11)$$

$Re_x = Re x/L$  is the local Reynolds number;  $Re = Lu/\nu$  is the Reynolds number;  $u$  is the free-stream velocity; and  $\nu$  is the fluid kinematic viscosity.

White is also the source of a widely used formula for turbulent skin-friction coefficient for smooth plates:

$$C_{f\sigma}(Re_x) = \frac{0.455}{\ln^2(0.06 Re_x)} \quad (12)$$

Mills and Hang [6] derived the average formula (10) from the local formula (9) by fitting a curve to the result of the numerical integration in formula (13):

$$\bar{C}_f \left( \frac{L}{k_S} \right) = \frac{k_S}{L - L_0} \int_{L_0/k_S}^{L/k_S} C_f(x) dx \quad (13)$$

The local formulas (7), (9), and (11) each have a singularity when the expression containing the logarithm is zero. The lower limit of integration ( $L_0/k_S$ ) must be large enough to avoid this, but the lower limit isn't revealed in the prior works. The averaging formula (13) is quite sensitive to the lower limit because the largest value of the local formula occurs there.

For the Mills-Hang formula (9), with a lower bound of 1.6 and initial  $dx/k_S = 0.01$ , integration of the local  $C_f$  is within  $\pm 0.5\%$  of the average  $\bar{C}_f$  in formula (10) over the range  $200 < x/k_S < 200 \times 10^3$ .

For the Prandtl-Schlichting formula (7), with a lower bound of 0.5 and initial  $dx/k_S = 0.5$ , integration of the local  $c_f$  is within  $\pm 0.5\%$  of the average  $\bar{c}_f$  in formula (8) over the range  $200 < x/k_S < 200 \times 10^3$ .

Churchill [9] compares 8 formulas from various sources with the data from Pimenta et al [5]; it doesn't find any to be significantly closer than the Mills-Hang local formula (9).

Churchill has different formulas for computing the average (mean) skin-friction  $C_m$  from local  $C_f$  for smooth and rough surfaces, respectively:

$$C_m = C_f \frac{1 - 4.516\sqrt{C_f}}{1 - 7.965\sqrt{C_f} + 21.52 C_f} \quad C_m = C_f \frac{1 - 4.516\sqrt{C_f}}{1 - 7.965\sqrt{C_f}} \quad (14)$$

## 5. Rough turbulence

Forced flow along a plate with a rough surface is different in character from forced flow along a smooth surface because roughness disrupts what would otherwise be a viscous sub-layer adjacent to the plate. Lienhard and Lienhard [16] teach: “Even a small wall roughness can disrupt this thin sublayer, causing a large decrease in the thermal resistance (but also a large increase in the wall shear stress).”

Jiménez [11] writes “In flows with  $\delta/k < 50$ , the effect of the roughness extends across the boundary-layer, and is also variable. There is little left of the original wall-flow dynamics in these flows, which can perhaps be better described as flows over obstacles.”

The present work focuses on this case where flow over obstacles dominates the dynamics. It does this by modeling rough turbulence as resulting from the interaction of bulk flow with a roughness which disrupts flow at a succession of scales from  $L$  (the length of the plate in the direction of flow) converging to 0. While simpler surfaces may also produce rough turbulence, a roughness which disrupts at this succession of scales surely will. Self-similarity will be used to succinctly describe this roughness across scales.

The turbulent boundary-layer thickness along a smooth plate increases proportionally to  $x^{4/5}$ , where  $x$  is the distance from its leading edge (Schlichting [7]). Roughness whose envelope height increases linearly with  $x$  can disrupt nascent boundary-layers repeatedly along the entire plate. This approach is a departure from prior works which relate the characteristic-length to boundary-layer thickness. Smooth turbulent, not rough turbulent, boundary-layers are analyzed in the present work. Except where stated otherwise, the characteristic-length  $L$  is the length of the plate in the direction of flow.

Although vortexes can arise in 2-dimensional systems, turbulence is a 3-dimensional phenomenon. Its random velocity fluctuations must be isotropic at all except the coarsest length scales. To guarantee this, the roughness should be “isotropic”; rotating the plate within its plane shouldn’t substantially affect the behavior of the system. A plate surface composed of parallel, edge-to-edge ridges and valleys wouldn’t satisfy this criterion. A quantitative test for isotropic roughness is developed in Section 12.

## 6. Profile roughness

Simpler than surface roughness, planar roughness profiles are nonetheless illustrative.

Let “profile roughness” be a function  $z(x)$  where  $0 \leq x \leq L$  is distance from the leading edge in the direction of flow up to plate length  $L$ . Given a roughness profile  $z(x)$ , its mean elevation  $\bar{z}$  and RMS height-of-roughness  $\epsilon$  (note symbol difference from surface roughness  $\varepsilon$ ) are:

$$\bar{z} = \frac{1}{L} \int_0^L z(x) dx \quad \epsilon = \sqrt{\frac{1}{L} \int_0^L |z(x) - \bar{z}|^2 dx} \quad (15)$$

Let “self-similar profile roughness” be a profile roughness function  $z(x)$  with (integer) branching factor  $n \geq 2$  such that the RMS height-of-roughness of  $z(x)$  over an interval  $x_0 < x < x_n$  is  $n$  times the RMS height-of-roughness of  $z(x)$  over each equally divided sub-interval  $x_t < x < x_{t+1}$  for  $0 \leq t < n$  at a succession of scales converging to zero. Note that each  $z(x_t)$  value contributes to its parent interval height-of-roughness, but not to any sub-interval.

A consequence of this definition is that the ratio of the length of an interval to the RMS height-of-roughness of  $z$  over that interval will be invariant over its succession of scales.

Of particular interest are self-similar roughness profiles which are permutations of the linear ramp  $z(x) = \varsigma x/L$  from  $x = 0$  to  $x = L$ , where  $\varsigma$  is the elevation of the highest peak. Every elevation from 0 to  $\varsigma$  occurs exactly once in a ramp-permutation. The only occurrence of  $x$  in formula (15) is  $z(x)$ ; hence the RMS height-of-roughness calculation depends only on the  $z$  values, not their relation to  $x$ . Thus, the height-of-roughness of any ramp-permutation is the same as the height-of-roughness of the ramp:

$$\epsilon = \sqrt{\frac{1}{L} \int_0^L \left[ \frac{\varsigma x}{L} - \frac{\varsigma}{2} \right]^2 dx} = \frac{\varsigma}{\sqrt{12}} \quad (16)$$

Similarly, all ramp-permutations have arithmetic-mean height-of-roughness  $\varsigma/4$ :

$$\frac{1}{L} \int_0^L \left| \frac{\varsigma x}{L} - \frac{\varsigma}{2} \right| dx = \frac{\varsigma}{4} \quad (17)$$

## 7. Self-similar ramp permutations

A self-similar integer sequence  $Y(t, w)$  of integers  $0 \leq t < w = n^q$  allows self-similar behavior to be explored with a finite approximation. Letting  $t = \lfloor wx/L \rfloor \equiv \text{floor}(wx/L)$  constructs a roughness profile from a sequence by  $z(x) = (\varsigma/w)Y(\lfloor wx/L \rfloor, w)$ . These three examples are  $n = 2$  ramp-permutation sequences:

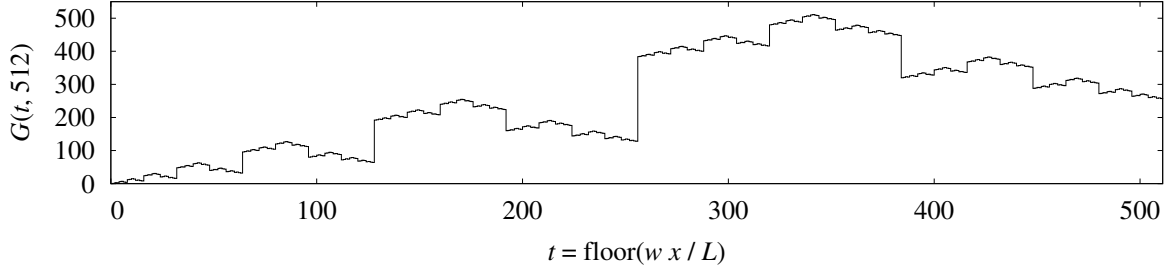


**Figure 2** Gray-code profile roughness

The integer Gray-code sequence  $G(t, w)$  shown in Figure 2 is a self-similar sequence defined by recurrence:

$$G(t, w) = \begin{cases} t, & \text{if } w = 1; \\ w + G(w - 1 - (t \bmod w), w/2), & \text{if } \lfloor t/w \rfloor = 1; \\ G(t \bmod w, w/2), & \text{otherwise.} \end{cases} \quad (18)$$

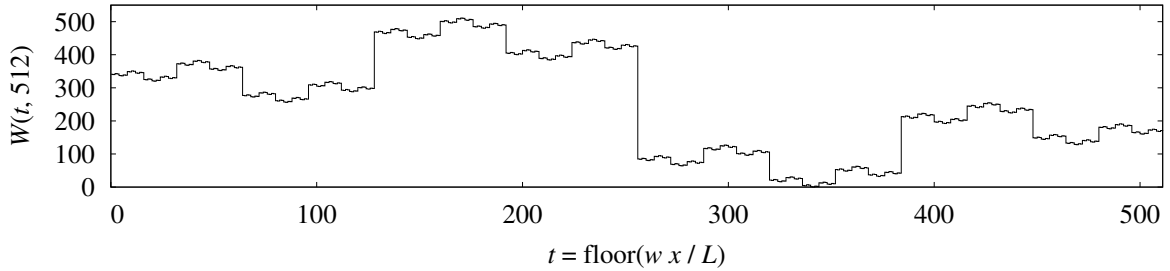


**Figure 3** wiggliest self-similar profile roughness

The integer sequence  $W(t, w)$  defined by recurrence (19) is shown in Figure 3; it reverses direction at each bifurcation, yielding a wiggliest possible self-similar ramp-permutation sequence.

$$W(t, w) = \begin{cases} t, & \text{if } w = 1; \\ \lfloor t/w \rfloor w + W(w - 1 - (t \bmod w), w/2), & \text{otherwise.} \end{cases} \quad (19)$$

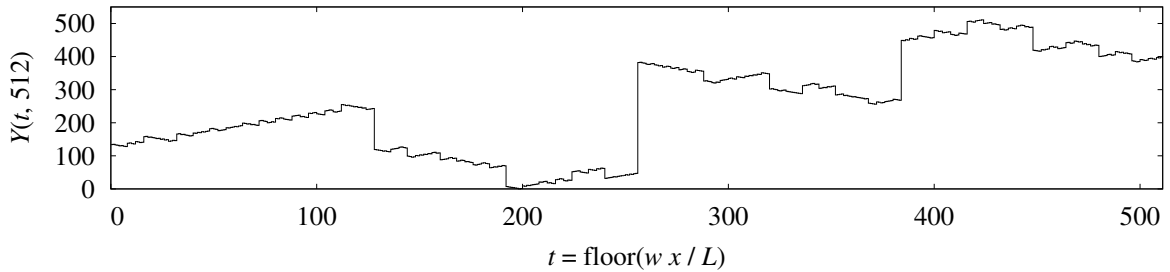


**Figure 4** random reversal bifurcation profile roughness

Figure 4 shows an integer sequence generated by recursive-descent, randomly reversing or not at each bifurcation (20); its roughness is self-similar by the definition of self-similar profile roughness in Section 6.

$$Y(t, w) = \begin{cases} t, & \text{if } w = 1; \\ w + Y(w - 1 - (t \bmod w), w/2), & \text{with probability 0.5;} \\ Y(t \bmod w, w/2), & \text{otherwise.} \end{cases} \quad (20)$$

For a given  $w = 2^q \geq 4$ , there are  $2^w = 2^{(2^q)}$  distinct self-similar ramp-permutation sequences, but only 2 distinct ramp and 2 distinct wiggliest sequences.

## 8. Roughness travel

In the conversion of flow to rough turbulence, particles of fluid must move in directions not parallel to the bulk flow. Such movement will result from deflection of flow by roughness peaks, ridges, and valleys; the amount of turbulence induced grows with the height-of-roughness.

Let “run” be the horizontal axis and “friction” be the vertical axis of a profile roughness such as is shown in Figure 4. For an integer ramp-permutation sequence  $Y(t, w)$ , the sum of the (dimensionless) lengths of all run segments is  $w - 1 = 2^q - 1$ . The sum of the absolute value of each friction segment length is:

$$\sum_{t=0}^{2^q-2} |Y(t, 2^q) - Y(t+1, 2^q)| \quad (21)$$

If a particle of fluid were to trace the ramp-permutation sequence  $Y(t, w)$  from  $t = 0$  to  $t = w - 1$ , then  $w - 1$  is the run distance it would travel, while formula (21) is the friction distance.

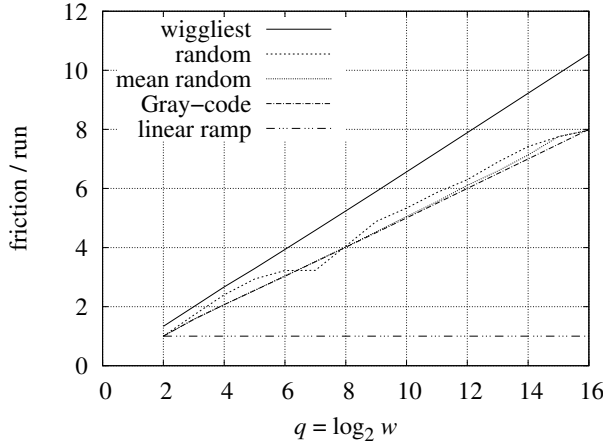


**Figure 5** travel along profile roughness

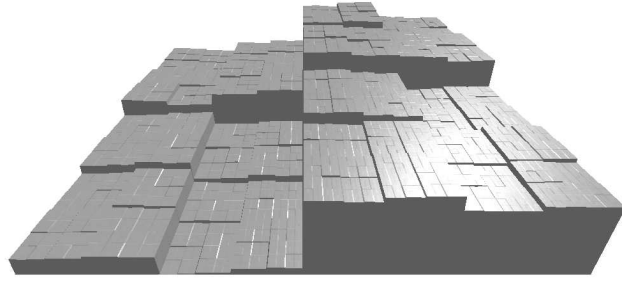


**Figure 6** random reversal ramp surface

Figure 5 shows the friction travel to run travel ratio versus  $q$ , the base-2 logarithm of  $w$ . The slope is 0 for the linear ramp, 1/2 for the Gray-code, approximately 1/2 for the random reversal cases, and 2/3 for the wiggliest roughness  $W$ .

A wiggliest roughness sequence  $W(t, w)$  is an extreme case; it reverses friction direction at each increment of run ( $t$ ). For each wiggliest roughness sequence with  $w \geq 4$  there are  $2^{w-1} - 2$  other random reversal roughness sequences. The linear ramp never reverses direction. For each linear ramp sequence there are  $2^{w-1} - 2$  other random reversal sequences. Being outliers,  $W(t, w)$  and linear ramps are excluded from further consideration as roughness.

In Figure 5, the friction to run ratios for Gray-code and random reversal sequences are close to:

$$\frac{q}{2} \equiv \frac{\log_2 w}{2} \quad (22)$$

$Y(t, w)$ ,  $t$ , and  $w$  are dimensionless. The friction to run ratio (22) needs to be reformulated in terms of the height-of-roughness. Turning to dimensional analysis, the argument to  $\log_2$  must be dimensionless, involve  $\epsilon$ , and be greater than 1, so that the logarithm will be positive. This ratio must increase with increasing  $\epsilon$ ; thus,  $\epsilon$  and the logarithm will be in denominators, yielding a friction travel to run travel ratio:

$$\frac{2}{\log_2(L/\epsilon)} \quad (23)$$

Scaling formula (23) by  $1/\sqrt{12}$  (from formula (16)) converts formula (23) into the ratio of RMS friction travel to run travel:

$$\frac{1}{\sqrt{12}} \frac{2}{\log_2(L/\epsilon)} = \frac{1}{\sqrt{3} \log_2(L/\epsilon)} \quad (24)$$



Considering the run travel and friction travel with respect to time lets formula (24) serve as the ratio of friction velocity  $u_\tau$  to bulk flow velocity  $u$ .

Newberry and Savage [17] demonstrate that some self-similar systems which are modeled using continuous power-law probability distributions can be modeled using discrete power-law distributions.

The present work uses their idea in reverse. The conversion of run velocity into friction velocity by contact with discrete self-similar  $n = 2$  roughness was modeled by formula (24); the conversion ratio for a random self-similar roughness will be inferred using a random variable.

Instead of summing  $|Y(t, 2^q) - Y(t + 1, 2^q)|$  as in formula (21), the analogous mean field theory is to integrate  $Z > 0$ , a continuous random variable having a Pareto distribution where the frequency of  $Z$  is inversely proportional to  $Z^2$ :

$$1 \left/ \left[ \sqrt{3} \int_\epsilon^L \frac{Z}{Z^2} dZ \right] \right. = \frac{1}{\sqrt{3} \ln(L/\epsilon)} \quad (25)$$

Travel along profile roughness is a planar path. Along self-similar surface roughness, an example of which is shown in Figure 6, the path of a particle can be 3-dimensional. In the generalization of formula (24) to random self-similar roughness in formula (25), the profile height-of-roughness  $\epsilon$  is replaced by the surface height-of-roughness  $\varepsilon$  defined in formula (3). As with profile RMS height-of-roughness, the surface RMS height-of-roughness of any permutation of the linear ramp from 0 to  $\varsigma$  is  $\varsigma/\sqrt{12}$ . Therefore, the  $1/\sqrt{3}$  coefficient doesn't change with the substitution of  $\varepsilon$  for  $\epsilon$  in formula (25).

### 9. Skin-friction from a rough plate

The skin-friction coefficient  $\overline{f}_c$  is the ratio of the shear stress  $\tau_2$ , which is primarily skin-friction drag when  $L/\varepsilon \gg 1$ , to the flow's kinetic energy density  $\rho u^2/2$ , where  $u$  is bulk flow velocity and  $\rho$  is fluid density:

$$\overline{f}_c = \frac{\tau_2}{\rho u^2/2} \quad (26)$$

Both  $\tau_2$  and  $\rho u^2/2$  have units of pressure,  $\text{kg}/(\text{m} \cdot \text{s}^2)$ ; hence  $\overline{f}_c$  is dimensionless. Multiplication by formula (25) converts bulk flow velocity  $u$  to friction velocity  $u_\tau$ , from which  $\tau_2$  is derived:

$$u_\tau = \frac{u}{\sqrt{3} \ln(L/\varepsilon)} \quad \tau_2 = \frac{\rho u_\tau^2}{2} = \frac{\rho u^2}{6 \ln^2(L/\varepsilon)} \quad \frac{L}{\varepsilon} \gg 1 \quad (27)$$

Combining equations (26) and (27) yields the formula for the average skin-friction coefficient  $\overline{f}_c$  of an isotropic self-similar rough surface:

$$\overline{f}_c = \frac{1}{3 \ln^2(L/\varepsilon)} \quad \frac{L}{\varepsilon} \gg 1 \quad (28)$$

Prandtl and Schlichting [1] calculates  $\tau = \rho u_\tau^2$ , not  $\tau_2 = \rho u_\tau^2/2$ . As a result, Prandtl-Schlichting  $\overline{C}_f$  is about twice  $\overline{f}_c$  of formula (28). Pimenta et al [5] and Mills and Hang [6] use  $\overline{C}_f/2$  as skin-friction coefficient. Equation (28) is compared with prior works in Section 21.

### 10. Skin-friction from a smooth plate

For a given  $Re \gg 1$  there must be a ratio  $L/\varepsilon$  so large that a plate of length  $L$  with self-similar roughness  $\varepsilon$  has turbulence-inducing behavior midway between that of a rough surface and that of a smooth surface.

Let the "roughness Reynolds number"  $Re_\varepsilon$  be the friction velocity  $u_\tau$  scaled to height-of-roughness  $\varepsilon$ :

$$Re_\varepsilon = \frac{u_\tau \varepsilon}{\nu} = \frac{u}{\sqrt{3} \ln(L/\varepsilon)} \frac{\varepsilon}{\nu} = \frac{Re}{\sqrt{3} [L/\varepsilon] \ln(L/\varepsilon)} \quad (29)$$

where  $\nu$  is the fluid kinematic viscosity and  $Re = Lu/\nu$ . The  $Re$  at which rough plate skin-friction transitions to smooth plate skin-friction will have the same  $Re_\varepsilon$  value at all  $L/\varepsilon \gg 1$ . Combining  $Re_\varepsilon = 1$  with formula (29) relates  $Re$  to  $L/\varepsilon$  at transition:

$$Re = \sqrt{3} \frac{L}{\varepsilon} \ln \frac{L}{\varepsilon} \quad (30)$$

Relation (30) between  $Re$  and  $L/\varepsilon$  suggests that the smooth turbulent skin-friction coefficient can be inferred from formulas (28) and (30). However, there being no roughness on a smooth plate,  $\overline{f_c}$  formula (28) must be adapted for this use; the  $L/\varepsilon$  argument to  $\overline{f_c}$  is scaled by  $1/e$ ; the value of  $\overline{f_c}$  is scaled by  $\sqrt[3]{2}$ :

$$\overline{f_{c\sigma}} = \sqrt[3]{2} \overline{f_c} \left( \frac{L}{e\varepsilon} \right) = \sqrt[3]{2} \left[ \frac{1}{3} \ln^{-2} \frac{L}{e\varepsilon} \right] \quad Re = \sqrt{3} \frac{L}{\varepsilon} \ln \frac{L}{\varepsilon} \quad (31)$$

$L/\varepsilon$  can be eliminated from formulas (31) using the Lambert W function. The inverse of  $\vartheta = \varphi \ln(\varphi)$  is  $\varphi = \exp(W_0(\vartheta))$ , where  $W_0$  is the principal branch of the Lambert W function.

$$\overline{f_{c\sigma}}(Re) = \frac{\sqrt[3]{2}}{3} \ln^{-2} \left( \frac{\exp(W_0(Re/\sqrt{3}))}{e} \right) = \frac{\sqrt[3]{2}/3}{[W_0(Re/\sqrt{3}) - 1]^2} \quad Re \gg \sqrt{3}e \quad (32)$$

Euler's number  $e = \exp(1)$  is a fixed point of  $\varphi \ln(\varphi)$  and its inverse,  $\exp(W_0(\vartheta))$ . The coefficient  $\sqrt[3]{2}/3 \approx 0.4200$ .  $Re \gg \sqrt{3}e \approx 4.71$  implies that smooth turbulence will not occur at  $Re < 100$ .

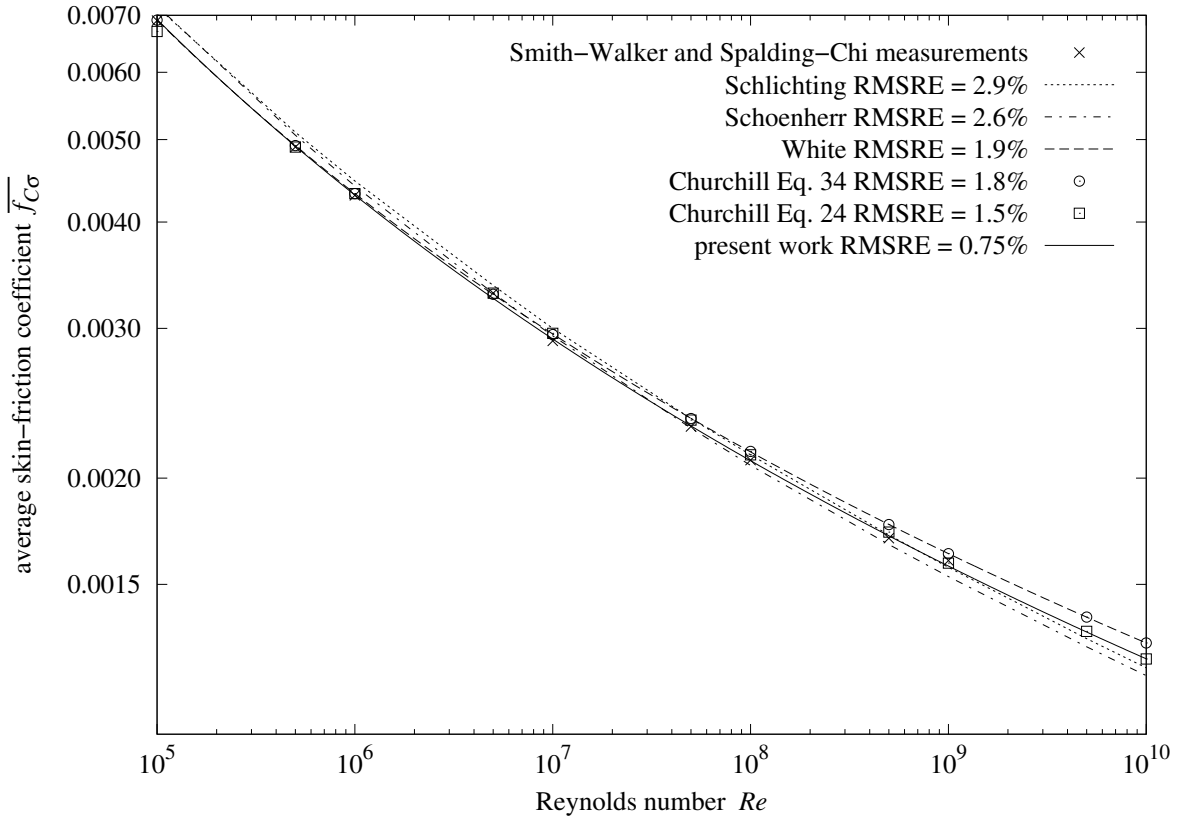


**Figure 7** average  $\overline{f_{c\sigma}}$  versus  $Re$  of smooth plate

Churchill [9] compares smooth turbulent skin-friction coefficient formulas from various sources with measured data from Smith and Walker [18], and Spalding and Chi [19]. Average formula and measured data values from Churchill [9] are shown in Figure 7. The “present work” formula (32) has 0.75% RMS relative error (RMSRE) from the “Smith-Walker and Spalding-Chi measurements”, significantly closer than any of the formulas evaluated by Churchill.

RMSRE gauges the fit of a formula  $f(Re)$  to data  $g(Re)$ , giving each measurement equal weight. The RMS error of  $f(Re)$  relative to  $g(Re)$  at  $n$  points  $Re_j$  is:

$$\sqrt{\frac{1}{n} \sum_{j=1}^n \left| 1 - \frac{f(Re_j)}{g(Re_j)} \right|^2} \quad (33)$$

## 11. Spectral roughness

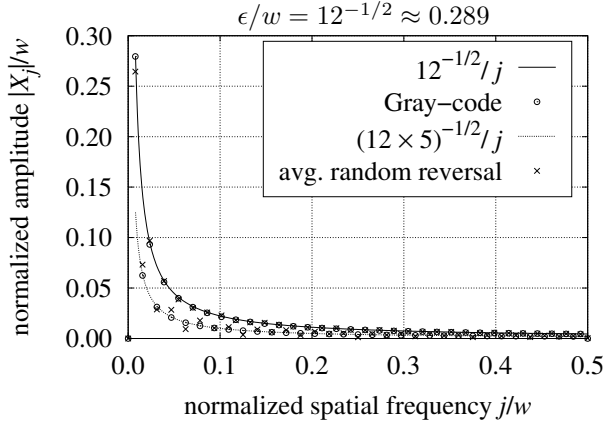
The concept of “uniform roughness” is incompatible with self-similarity; the RMS height-of-roughness of a portion of a self-similar surface must shrink with the succession of scales converging to 0.

A roughness composed of repeated patches having the same mean elevation  $\bar{z}$  and height-of-roughness  $\epsilon$  could be called uniform roughness, whether the patches are self-similar or not. The composite plate has the same  $\bar{z}$  and  $\epsilon$  as the patches. But the behavior of the plate might depend on the size of the patches. An unambiguous method for determining the spatial period is needed.

The discrete Fourier transform converts a series of equally-spaced samples of a (roughness) function into complex coefficients for each of its sinusoidal components. There is a profound connection between the discrete Fourier transform  $X_j$  of a roughness sequence  $Y(t, w)$  and its RMS height-of-roughness  $\epsilon$ :

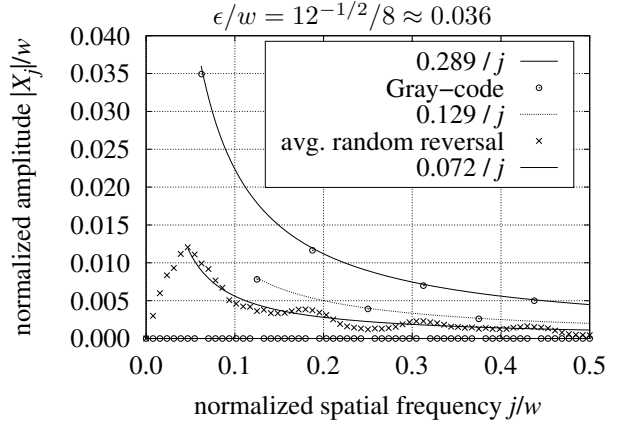
$$X_j = \sum_{t=0}^{w-1} Y(t, w) \exp\left(\frac{-2\pi i j t}{w}\right) \quad \epsilon = \sqrt{\frac{1}{w} \sum_{j=1}^{w-1} |X_j|^2} \quad (34)$$

Note that constant term  $X_0 = \bar{z}$ , the mean value of  $Y$ , is the only  $X_j$  term not included in the sum for  $\epsilon$ . Because  $\epsilon$  doesn't depend on  $X_0$ , for  $0 < j < w/2$ , the  $X_j$  with the largest amplitude is the dominant contributor to roughness, and has a normalized spatial frequency  $j/w$ ; let the “period index”  $j_P$  be the  $j$  of this largest amplitude  $X_j$ .



**Figure 8** Gray and random spectra

Figure 8 shows the  $|X_j|/w$  spectrum of the Gray-code roughness profile (Figure 2), and the averaged Fourier spectrum amplitudes from 187 instances of 128-point random reversal profiles. For both spectra,  $X_1$  has the largest amplitude; thus  $j_P = 1$ , indicating that neither spectrum is from repeated roughness.



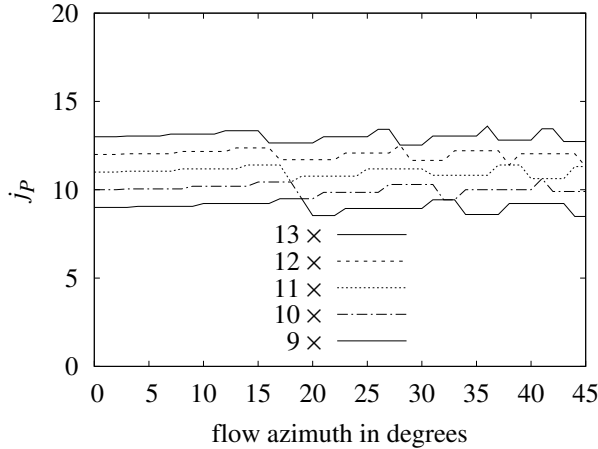
**Figure 9** Gray and random eighths

Figure 9 shows the spectrum of eight concatenated repetitions of a Gray-code sequence, and the averaged Fourier spectrum amplitudes from 187 instances of eight concatenated random reversal sequences. The period index  $j_P$  of Gray-code eighths is 8, as expected, but the random reversal sequences have  $j_P = 6$  because the amplitudes aren't correlated between the random eighths.

This method looks promising for detecting and quantifying roughness periods when  $j_P \gg 1$ , but the present theory also requires that surface roughness be isotropic.

## 12. Periodic roughness

Let a surface with “periodic roughness” be an array of many isotropic, uniformly sized patches, all sharing the same mean elevation  $\bar{z}$  and RMS height-of-roughness  $\varepsilon$ .



**Figure 10** bi-level plate 50%

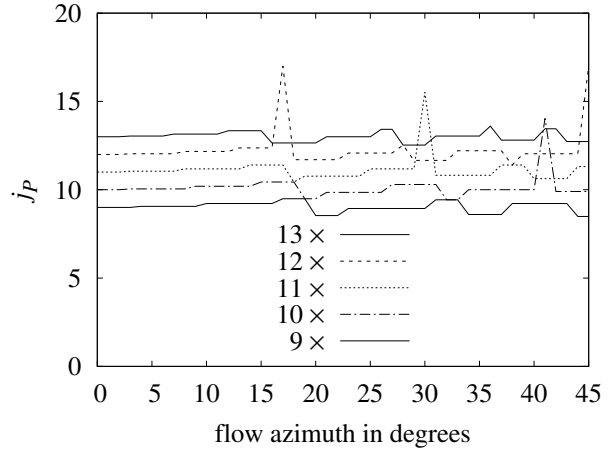


**Figure 11** bi-level plate 25%

The spatial period  $L_P = L/j_P = L/\sqrt{j^2 + k^2}$ , where  $j, k$  are the indexes of the (2-dimensional)  $w \times w$  discrete spatial Fourier transform coefficient  $X_{j,k}$  with the largest amplitude. Figure 10 shows  $j_P = \sqrt{j^2 + k^2}$  for a square equal-area bi-level surface (regular array of square posts on flat plate) computing  $X_{j,k}$  from a  $64 \times 64$  interpolated sampling of that surface with azimuth from  $0^\circ$  through  $45^\circ$  scaled between 9 and 13 cells on a side. At each scale,  $j_P$  varies within a  $\pm 1$  range versus the azimuth. Figure 11 shows a 25% high, 75% low, bi-level surface; its  $j_P$  varies more than  $\pm 1$ . This suggests a quantitative criterion for roughness isotropy:

A surface roughness is isotropic if  $j_P = L/L_P$  varies no more than  $\pm w/32$  through its full rotation.

More specifically, using  $w \times w$  ( $w = 64, 128$ ) samplings of roughness with randomized periods between  $8/w$  and  $16/w$ , randomized offset, and random azimuth, a roughness is considered isotropic if no more than 5 of 500 trials have  $j_P$  varying more than  $\pm w/32$ .

Using this criterion, square post arrays having upper area fraction between 27% and 76% are isotropic. Square arrays of circular columns having upper area fraction between 24% and 78% are isotropic. Hexagonal arrays of circular columns having upper area fraction between 6% and 75% are isotropic. The complement, hexagonal arrays of circular depressions in an otherwise flat, smooth plate having upper area fraction between 25% and 94% are isotropic.

Plates with stretched (15%) hexagonal arrays of cone and bump protrusions described in Schlichting [3] are also isotropic;  $L_P$  in this case is the geometric mean of the periods of the stretched axis and an axis perpendicular to it.

The visual appearance of isotropy and this test for isotropy are not equivalent. Square post arrays having upper area fractions of 20% don't pass the isotropy test, while those with 30% do. Plates from Schlichting [3] having stretched hexagonal arrays of cones aren't visually isotropic, but pass the isotropy test.

### 13. Onset of rough turbulence

For an isotropic periodic roughness with  $0 < \varepsilon < L_P \ll L$ , there must be some value of  $Re > 0$  less than which the flow exhibits laminar or smooth turbulent behavior along the entire plate. The boundary-layer is thinnest at the leading edge. If the boundary-layer is going to be disrupted, then it will start within the leading band ( $0 < x < L_P$ ) of periodic roughness. In the present work, a boundary-layer is considered disrupted when  $\varepsilon > \delta_2(L_P)$ , where  $\delta_2(x)$  is the boundary-layer momentum thickness at  $x$ .

$\delta_2(x)$  is the thickness of bulk flow having the same momentum flow rate as the plate boundary-layer at  $x$ . Momentum thickness  $\delta_2$  isn't a directly measurable quantity. Schlichting [7] gives the momentum thickness of laminar and smooth turbulent boundary-layers as  $\delta_{2\lambda}(x) = 0.664 x Re_x^{-1/2}$  and  $\delta_{2\sigma}(x) = 0.036 x Re_x^{-1/5}$ , respectively. The local Reynolds number  $Re_x = Re x/L$ . Equivalently, the laminar and smooth turbulent boundary-layer thicknesses are:

$$\delta_{2\lambda}(x) = 0.664 \sqrt{Re_x} \frac{L}{Re} \quad \delta_{2\sigma}(x) = 0.036 Re_x^{4/5} \frac{L}{Re} \quad (35)$$

The laminar flow  $\delta_{2\lambda}$  is from the Blasius boundary-layer model, which is well supported by measurement. The smooth turbulent  $\delta_{2\sigma}$  formula is less certain. Continuing analysis of smooth turbulent skin-friction, with free variable  $\varepsilon$ , combine roughness Reynolds number  $Re_\varepsilon$  formula (29) with  $Re_\varepsilon = L/x$  (instead of  $Re_\varepsilon = 1$ ) and solve for  $L/\varepsilon$ :

$$\frac{Re x}{\sqrt{3} L} = \frac{L}{\varepsilon} \ln \frac{L}{\varepsilon} \quad \frac{L}{\varepsilon} = \exp \left( W_0 \left( \frac{Re x}{\sqrt{3}} \right) \right) \quad (36)$$

The smooth turbulence momentum thickness  $\delta_2(x)$  should be proportional to the product of  $x$  (distance from the leading edge) and the ratio of friction velocity  $u_\tau$  from formula (27) to bulk flow velocity  $u$ :

$$\delta_2(x) \propto x \frac{u_\tau}{u} = \frac{x}{\sqrt{3} \ln(L/\varepsilon)} = \frac{x}{\sqrt{3} W_0(Re_x/\sqrt{3})} \quad (37)$$

The coefficient seems to be  $1/3^3 = 1/27 \approx 0.0370$ , which may be related to  $\exp(\varphi \ln(\varphi)) \equiv \varphi^\varphi$ .

$$\delta_2(x) = \frac{x}{3^3 W_0(Re_x/\sqrt{3})} \quad Re_x \gg \sqrt{3} e \quad (38)$$

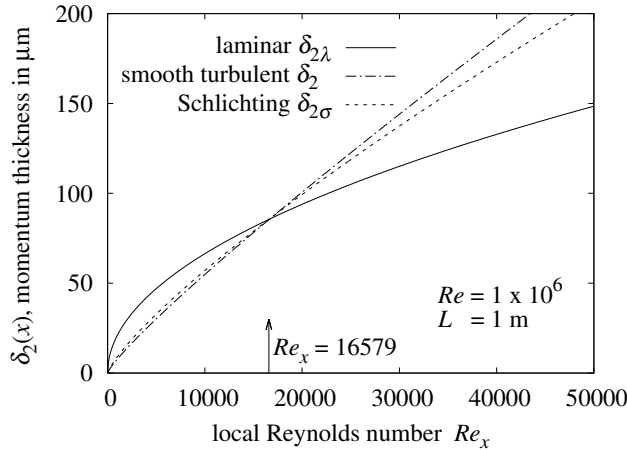


**Figure 12** smooth plate  $\delta_2(x)$  versus  $Re_x$

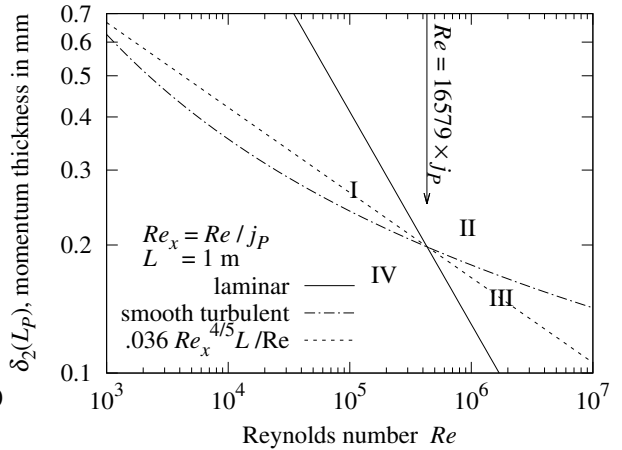


**Figure 13** smooth plate  $\delta_2(L_P)$  versus  $Re$

Figure 12 demonstrates that “smooth turbulent  $\delta_2$ ” from equation (38) and  $\delta_{2\sigma}$  from equation (35) are close to each other between the origin and the intersection of the laminar and turbulent curves at:

$$0.664 \sqrt{Re_x} = 0.036 Re_x^{4/5} \quad Re_x = \left[ \frac{0.664}{0.036} \right]^{10/3} \approx 16579 \quad (39)$$

Because  $L_P \ll L$ , when  $x = L_P$ , then  $Re_x \ll Re$ ; hence,  $\delta_{2\sigma}(L_P)$  is a reasonable approximation for  $\delta_2(L_P)$  in the leading band of roughness.

Figure 13 shows the theoretical momentum thickness of laminar and smooth turbulent flows along a 1 m long plate versus  $Re$ . The laminar  $\delta_{2\lambda}$  and smooth turbulent  $\delta_2$  curves divide the graph into four regions. When the point at coordinates  $[Re, \varepsilon]$  is in regions I or IV, then it won't significantly disrupt laminar flow; hence, the flow along the plate will be laminar. When  $[Re, \varepsilon]$  is in region II, then its height is sufficient to disrupt both laminar and smooth turbulent flow; so the flow along the plate will be rough turbulent.

When  $[Re, \varepsilon]$  is in region III, then the roughness would be sufficient to disrupt laminar flow, but not large enough to disrupt smooth turbulent flow; so the flow along the plate would be smooth turbulent.

With  $\delta_{2\lambda} = \varepsilon$  and  $x = L_P$ , solve  $\delta_{2\lambda}$  formula (35) for laminar upper-bound  $Re_\lambda$ :

$$Re_\lambda = \left[ \frac{0.664}{\varepsilon} \right]^2 L_P L \quad (40)$$

With  $\delta_2 = \varepsilon$  and  $x = L_P$  in formula (38):

$$\varepsilon = \frac{L_P}{3^3 W_0 (Re L_P / (\sqrt{3} L))} \quad W_0 \left( \frac{Re L_P}{\sqrt{3} L} \right) = \frac{L_P}{3^3 \varepsilon} \quad Re \gg \frac{\sqrt{3} e L}{L_P} \quad (41)$$

The inverse of  $\varphi = W_0(\vartheta)$  is  $\vartheta = \varphi \exp(\varphi)$ . Solving for  $Re$ :

$$\frac{Re L_P}{\sqrt{3} L} = \frac{L_P}{3^3 \varepsilon} \exp \frac{L_P}{3^3 \varepsilon} \quad Re_\sigma = \frac{\sqrt{3} L}{3^3 \varepsilon} \exp \frac{L_P}{3^3 \varepsilon} \quad (42)$$

Equating  $Re_\lambda$  and  $Re_\sigma$  yields their intercept:

$$\left[ \frac{0.664}{\varepsilon} \right]^2 L_P L = \frac{\sqrt{3} L}{3^3 \varepsilon} \exp \frac{L_P}{3^3 \varepsilon} \quad \frac{L_P}{\varepsilon} \approx 194.3 \quad (43)$$

To reach region III requires a plate with repeated roughness ratio  $L/\varepsilon > 25 L_P/\varepsilon > 4858$ . The machining precision must be substantially finer than this in order for the roughness of each patch to be significantly larger than the residual elevation error. Region III smooth turbulent flow will be rare; otherwise, flow along periodic roughness will transition directly from laminar to rough turbulent as  $Re > Re_\lambda$ .

Lienhard [20] models a gradual transition from laminar to smooth turbulence along smooth plates. In contrast, for periodic roughness the transition will be abrupt because it takes place in the leading band of roughness, where the slope of the laminar boundary-layer thickness curve is steepest.

#### 14. Flat-peaked roughness

A smooth turbulent boundary layer can form along an isotropic periodic rough surface when  $Re_\lambda < Re < Re_\sigma$ , or when the peaks of the roughness are all co-planar flats. In the latter case, the smooth turbulent flow occurs downwind from where  $x$  is large enough for the boundary layer (which grows with  $x$ ) to bridge the gaps. The drag from the downwind portion of such a surface will be proportional to  $\overline{f_{c\sigma}}$ , not the constant coefficient  $\overline{f_c}$  of rough turbulent flow, making it an instance of a non-constant terminal drag coefficient as described by Dr. Hoerner in Hama [4] (see present work Section 1).

Let a “flat-peaked roughness” be an isotropic periodic roughness where each cell contains a contiguous flat-peak area whose boundary has a convex perimeter within the cell, and all the flat-peak areas are at the same elevation.

For a flat-peaked roughness, let “openness”  $0 < \Omega < 1$  be the ratio of non-peak area to cell area;  $1 - \Omega$  will thus be the ratio of peak area to cell area.

Consider a smooth flat plate etched with a square grid of grooves subjected to a moderate flow parallel to its surface. When the boundary-layer is disrupted by a groove perpendicular to the flow, the smooth turbulent boundary-layer restarts at the edge of the flat-peak. At the scale of the roughness period  $L_P$ , the momentum thickness of the boundary-layer grows from 0 to nearly (depending on how long the flat is) the  $L$ -scale  $\delta_2(x)$  value. If it grows to exceed  $\varepsilon$ , then the rest of the plate (to its trailing edge) will have a smooth turbulent skin-friction coefficient proportional to  $\overline{f_{c\sigma}}$ .

For isotropic roughness, the growth of  $\delta_2$  depends on the size of the flat-peaks, but not on their orientation with respect to flow. In natural convection from an upward-facing horizontal plate [21, 22], the isotropic characteristic-length metric  $L_*$  is the ratio of the convex region area to its perimeter. For a regular polygon or circle,  $L_* = r/2$ , where  $r$  is the minimum radius of the regular polygon or circle.

Multiplying both sides of  $\delta_2$  formula (38) by  $3^3 Re / (\sqrt{3} L)$  allows  $Re_x$  to be isolated using the Lambert  $W_0$  function identity  $\varphi/W_0(\varphi) = \exp W_0(\varphi)$ :

$$\frac{3^3 Re}{\sqrt{3} L} \delta_2 = \frac{Re_x / \sqrt{3}}{W_0(Re_x / \sqrt{3})} \quad \frac{3^3 Re}{\sqrt{3} L} \delta_2 = \exp W_0 \left( \frac{Re_x}{\sqrt{3}} \right) \quad (44)$$

Let  $\delta_2 = \varepsilon$  in order to find the  $Re_x$  threshold  $Re_i$ . Turning to dimensional analysis, the  $Re$  flow rate needed to produce smooth turbulence grows with  $\varepsilon/L_*$  and with  $L/L_P$ . Substituting a product of powers of these ratios for  $Re$  and taking logarithm of both sides of equation (44):

$$Re = \frac{\varepsilon}{L_*} \left[ \frac{L}{L_P} \right]^3 \quad \ln \frac{3^3 \varepsilon^2 L^2}{\sqrt{3} L_* L_P^3} = W_0 \left( \frac{Re_x}{\sqrt{3}} \right) \quad (45)$$

The inverse of  $\varphi = W_0(\vartheta)$  is  $\vartheta = \varphi \exp(\varphi)$ :

$$Re_i = Re_x = \frac{3^3 \varepsilon^2 L^2}{L_* L_P^3} \ln \frac{3^3 \varepsilon^2 L^2}{\sqrt{3} L_* L_P^3} \quad \frac{[4 L_*]^2}{L_P^2} > \frac{1}{2} \quad (46)$$

Formula (46) is tested against a plate with  $[4 L_*]^2 / L_P^2 > 1/2$  in Section 26.

When a perforated sheet is laid on a flat plate, the holes in the sheet become wells.  $L_*$  is the ratio of the hole area to its perimeter. The flow along the perforated sheet must return to the upper level after diving into a well; hence, there are twice as many roughness interactions per cell. Instead of  $Re = [\varepsilon/L_*] [L/L_P]^3$  in formula (45), let:

$$Re = \frac{\varepsilon}{L_*} \left[ \frac{L}{2 L_P} \right]^3 \quad \ln \frac{3^3 \varepsilon^2 L^2}{\sqrt{3} 2^3 L_* L_P^3} = W_0 \left( \frac{Re_x}{\sqrt{3}} \right) \quad (47)$$

leading to the  $Re_x$  threshold  $Re_w$ .

$$Re_w = \frac{3^3 \varepsilon^2 L^2}{2^3 L_* L_P^3} \ln \frac{3^3 \varepsilon^2 L^2}{\sqrt{3} 2^3 L_* L_P^3} \quad \frac{[4 L_*]^2}{L_P^2} < \frac{1}{2} \quad (48)$$

The inequality is reversed for formula (48) because this convex perimeter is filled with non-peak instead of flat-peak area. Formula (48) and its inequality are tested against three perforated sheets in Section 25.

## 15. Bi-level roughness

An important class of flat-peaked roughness is bi-level roughness, which has only two distinct elevations. Let  $\varepsilon_{pv}$  be the absolute value of the difference between the two elevations.

$$\bar{z} = [1 - \Omega] \varepsilon_{pv} \quad \varepsilon = \sqrt{(\varepsilon_{pv} - \bar{z})^2 [1 - \Omega] + \bar{z}^2 \Omega} = \varepsilon_{pv} \sqrt{[1 - \Omega] \Omega} \quad (49)$$

All of the flat-peaked roughness measurements cited or performed in the present work were from plates having bi-level roughness.

## 16. Flow modes

The flow along isotropic periodic roughness can be multi-modal when that roughness is flat-peaked.

condition	flat-peaked islands	flat-peaked wells	not flat-peaked
$Re < Re_\lambda$	laminar	laminar	laminar
$Re_\lambda < Re < Re_\sigma$	smooth?	smooth?	smooth?
$[4L_*]^2/L_P^2 > 1/2$		rough	rough
$Re_x < Re_w$		mix formula (50)	rough
$Re_x > Re_w$		smooth formula (52)	rough
$[4L_*]^2/L_P^2 < 1/2$	rough?		rough
$Re_x < Re_i$	rough		rough
$Re_x > Re_i$	smooth formulas (53, 54)		rough

**Table 2** flow modes for isotropic periodic roughness

Table 2 shows the flow modes for the periodic configurations of plate roughness treated by the present theory. Plates must be isotropic and periodic, as determined by the Fourier-transform based method of Section 12, and satisfy  $\varepsilon < L_P \ll L$ . Sand-roughness, the sphere roughness of Pimenta et al, and random surfaces qualify as “not flat-peaked”.

The uppermost flow mode satisfying the condition on its left takes precedence for the column. The  $Re_x$  conditions split the plate at distance  $x$  from the leading edge into two regions operating in different modes simultaneously.

“Smooth” and “rough” refer to smooth turbulence and rough turbulence, respectively. In “mix” mode for flat-peaked wells, the perforated sheet upper surface is in smooth turbulence, while the wells are in rough turbulence. The effective friction coefficient is the area-proportional mix:

$$\Omega \overline{f_c}(L/\varepsilon) + [1 - \Omega] \overline{f_{c\sigma}}(Re) \quad (50)$$

Where  $Re_x > Re_w$  along a perforated sheet, the friction is smooth turbulent, but with additional area from the rims. The areas combine as the  $\ell^2$ -norm (equivalent to root-sum-squared), which is the  $\ell^p$ -norm formula (51) with  $p = 2$ :

$$\|\varphi, \vartheta\|_p = (|\varphi|^p + |\vartheta|^p)^{1/p} \quad (51)$$

$$\left\| 1, \sqrt{6} \frac{3\varepsilon [4L_*]}{L_P^2} \right\|_2 \overline{f_{c\sigma}}(Re) = \sqrt{1 + 6 \left[ \frac{3\varepsilon [4L_*]}{L_P^2} \right]^2} \overline{f_{c\sigma}}(Re) \quad (52)$$

The coefficient  $3\sqrt{6} = \sqrt{2}\sqrt{3^3} \approx 7.348$ . Measurements of perforated sheets are compared with formulas (50) and (52) in Section 25.

The “ $Re_x > Re_i$ ” condition for flat-peaked islands is smooth turbulence with characteristic-length scaled to  $L_P$ . The flat-peaked area of the island is augmented by one third of the non-peak area combined with  $2\varepsilon [4L_*]$  using the  $\ell^2$ -norm:

$$\left\{ 1 - \Omega + \left\| \frac{\Omega}{3}, \frac{2\varepsilon [4L_*]}{L_P^2} \right\|_2 \right\} \overline{f_{c\sigma}} \left( \frac{Re L_P}{L} \right) \quad (53)$$

$$\left\{ 1 - \Omega + \left\| \frac{\Omega}{3}, \frac{2\varepsilon [4L_*]}{L_P^2} \right\|_2 \right\} \frac{L}{L_P} \overline{Nu_\sigma} \left( \frac{Re L_P}{L} \right) \quad (54)$$

Convection measurements from a square grooved bi-level plate are compared with formula (54) in Section 26.

Measurements from a grooved plate with dimensions satisfying  $[4L_*]^2/L_P^2 < 1/2$  are lacking; it is designated “rough?” in Table 2. Also lacking is a plate meeting the stringent requirements described in Section 13 for operation in Region III of Figure 13; the entire  $Re_\lambda < Re < Re_\sigma$  row is designated “smooth?”.



## 17. Local skin-friction

Conversions between local and average skin-friction are needed in order to compare prior with present work.

The ratio of average to local skin-friction  $\overline{f_c}/f_c > 1$  of a continuous boundary-layer is calculated from local skin-friction coefficient  $f_c$  by formula (55). The singularity (division by 0) at the leading edge of the plate is avoided by using  $Re_0 > 0$  as the integration lower bound;  $Re_0$  must be chosen such that  $f_c(Re_0) \ll 1$ .

$$\frac{\overline{f_c}(Re)}{f_c(Re)} = \frac{1}{Re - Re_0} \int_{Re_0}^{Re} \frac{f_c(Re_x)}{f_c(Re)} dRe_x \quad (55)$$

The local skin-friction coefficient  $f_c$  isn't well-defined for self-similar roughness because its  $L/\varepsilon$  is constant. Periodic roughness has varying  $L/\varepsilon$ ; it also provides  $L_P/\varepsilon$  as the lower bound of integration.

A crucial difference between periodic roughness and smooth surfaces is that periodic roughness disrupts the boundary-layer repeatedly. Thus, the local skin-friction coefficients being averaged are independent; instead of  $\overline{f_c}/f_c$  accruing linearly, it should go as the square:

$$\frac{\overline{f_c}(L/\varepsilon)}{f_c(L/\varepsilon)} = \left[ \frac{\varepsilon}{L - L_P} \int_{L_P/\varepsilon}^{L/\varepsilon} \frac{f_c(r)}{f_c(L/\varepsilon)} dr \right]^2 \quad (56)$$

Applying formula (56) to the Mills-Hang local formula (9) yields the average skin-friction coefficient:

$$\overline{C_f}^2 / C_f \quad (57)$$

where  $C_f$  and  $\overline{C_f}$  are from equations (9) and (10), respectively.

At  $L/\varepsilon = 4000$  ( $L/k_S = 750$ ), formula (57) has values in excess of 20% larger than the Mills-Hang  $\overline{C_f}$  formula (10) derived using averaging formula (13). The average skin-friction coefficient was of minor importance in Mills and Hang [6]; they didn't compare with measurements of average skin-friction.

For a disrupted boundary-layer, the transform for local friction  $f_c$  given average friction  $\overline{f_c}$  is:

$$\frac{f_c(L/\varepsilon)}{\overline{f_c}(L/\varepsilon)} = \left[ \frac{d([L - L_P] \overline{f_c}(L/\varepsilon))}{dL} \bigg/ \overline{f_c}(L/\varepsilon) \right]^2 \quad (58)$$

Applying formula (58) to  $\overline{f_c}$  formula (28) for rough surfaces yields the local skin-friction coefficient:

$$f_c(x/\varepsilon) = \frac{1}{3} \left[ \frac{\ln(x/\varepsilon) + 2[L_P/x - 1]}{\ln^2(x/\varepsilon)} \right]^2 \quad L \geq x > L_P \geq \varepsilon \quad (59)$$

The local skin-friction coefficient for smooth turbulent flow can be derived from  $\overline{f_{c\sigma}}$  equation (32) and equations (60) with  $Re_x \geq Re_0 \geq \sqrt{3}e$  and  $Re_x \gg \sqrt{3}e$ :

$$\frac{dW_0(\vartheta)}{d\vartheta} = \frac{W_0(\vartheta)}{\vartheta [W_0(\vartheta) + 1]} \quad f_{c\sigma}(Re_x) = \frac{d([Re_x - Re_0] \overline{f_{c\sigma}}(Re_x))}{dRe_x} \quad (60)$$

$$f_{c\sigma}(Re_x) = \frac{\sqrt[3]{2} W_0^2(Re_x/\sqrt{3}) - 2[1 - Re_0/Re_x] W_0(Re_x/\sqrt{3}) - 1}{3 [W_0(Re_x/\sqrt{3}) - 1]^3 [W_0(Re_x/\sqrt{3}) + 1]} \quad (61)$$

Local smooth turbulent skin-friction coefficient formulas and data values provided by Churchill [9] are shown in Figure 14. The ‘‘present work’’ formula (61) has 2% RMS relative error (RMSRE) from the ‘‘Smith-Walker and Spalding-Chi measurements’’.

Note that when calculating RMSRE, the increase from a variation at a single point is larger than the increase when that variation is split among multiple points. Thus, local measurements tend to have larger RMSRE than average measurements. In Figure 14, the primary error contributor is the value at  $Re_x = 10^7$ .

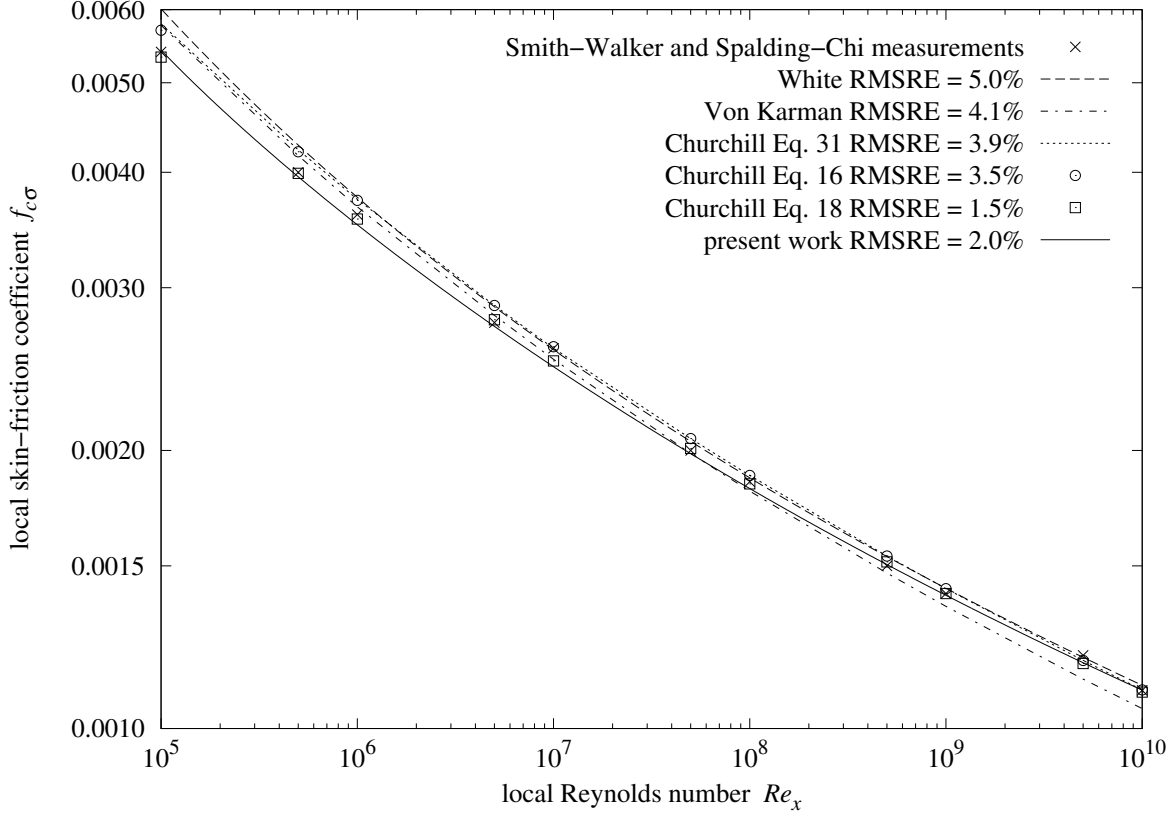


Figure 14 local  $f_{c\sigma}$  versus  $Re_x$  of smooth plate

### 18. Forced convection from a rough plate

Forced convective heat transfer is expressed as the dimensionless average ( $\overline{Nu}$ ) or local ( $Nu$ ) Nusselt number. Heat transfer by rough turbulence will grow with the amount of turbulence induced,  $\overline{f_c} Re$ . It will also grow with the fluid's Prandtl number ( $Pr$ ), the ratio of kinetic viscosity to thermal diffusivity. Fluids with large  $Pr$  transport heat in the fluid flow; conduction is dominant in fluids with small  $Pr$ . The  $1/3$  exponent for  $Pr$  may relate to it being a property of the fluid in three dimensions. Heat transfer from the trailing part of the plate is reduced due to fluid heating by the leading part; hence, formula (62) is scaled by  $1/2$ . Expanding  $\overline{f_c}$  from equation (28) yields formula (62) for rough turbulent average forced convection:

$$\overline{Nu} = \frac{\overline{f_c} Re Pr^{1/3}}{2} = \frac{Re Pr^{1/3}}{6 \ln^2(L/\varepsilon)} \quad \frac{L}{\varepsilon} \gg 1 \quad Pr > 0 \quad (62)$$

The analysis for self-similar  $\overline{f_c}$  didn't involve boundary-layers; hence, there is no restriction to  $Pr > 0.6$ . Formula (62) is compared with measurements in Section 26.

### 19. Forced convection from a smooth plate

For smooth turbulent convection, Lienhard [20] recommends composing the Gnielinski formula (63) with the White smooth formula (12) for  $C_{f\sigma}$ . Note that formula (63) is local convection ( $Nu$ ).

$$Nu = \frac{Re_x Pr C_{f\sigma}/2}{1 + 12.7 [Pr^{2/3} - 1] \sqrt{C_{f\sigma}/2}} \quad Pr \geq 0.6 \quad (63)$$

Lienhard states that  $Nu$  formula (64) has similar accuracy for gases:

$$Nu = 0.0296 Re_x^{4/5} Pr^{0.6} \quad \overline{Nu} = 0.037 Re^{4/5} Pr^{0.6} \quad (64)$$

Natural convection from a vertical plate is similar to forced convection; in both, the flow is uniform along the plate's characteristic-length  $L$ .

Jaffer [23] finds that stationary fluid conducts heat from the plate with an effective Nusselt number  $Nu_0$ :

$$Nu_0 = \frac{16}{\pi^2 \sqrt[4]{2}} \approx 1.364 \quad (65)$$

The flow-induced heat transfer will grow with  $Nu_0 Re \overline{f_{c\sigma}}$ . Because heat must traverse boundary-layers, the smooth convection dependence on  $Pr$  is more complicated than  $\sqrt[3]{Pr}$ . In Jaffer [23], the vertical-plate natural convection  $\overline{Nu}$  dependence on  $Pr$  is  $\sqrt[3]{Pr/\Xi}$ , where  $\Xi(Pr)$  is defined using the  $\ell^p$ -norm formula (51) with  $p = \sqrt{1/3}$ :

$$\Xi(Pr) = \left\| 1, \frac{0.5}{Pr} \right\|_{\sqrt{1/3}} \quad \|\varphi, \vartheta\|_p = (|\varphi|^p + |\vartheta|^p)^{1/p} \quad (66)$$

Figure 15 shows that  $\sqrt[3]{Pr/\Xi}$  is asymptotically  $\sqrt[3]{Pr}$  for large  $Pr$  and  $\sqrt[3]{2} Pr^{2/3}$  for small  $Pr$ . At small  $Pr$ , conduction doesn't amplify forced convection as it does natural convection; the  $Pr$  exponent should be 1. An additional factor using the  $\ell^3$ -norm accomplishes this. Formula (67) is asymptotically  $\sqrt[3]{2} Pr$  at  $Pr < 0.5$ . The “0.7  $Pr^{0.6}$ ” trace shows that formula (67) has a slope close to formula (64) for gases.

$$\sqrt[3]{\frac{Pr}{\Xi}} \sqrt[3]{\frac{1}{\|1, 1/Pr\|_3}} \quad (67)$$

The slope of formula (63)  $Nu(Re_x)$  decreases with increasing  $Pr$ ; for large  $Pr$ ,  $Nu \propto \sqrt{C_{f\sigma}}$ . Recall from equations (26) and (27) that  $\sqrt{f_c}$  is proportional to friction velocity  $u_\tau$ ; this indicates that transport through the boundary-layer limits convection at large  $Pr$ . In order to reduce asymptotic dependence from  $\overline{f_{c\sigma}}$  to  $\sqrt{f_{c\sigma}}$ , convection will include a factor taking square-root of an expression gating  $1/\overline{f_{c\sigma}}$  by  $Pr$ :

$$\sqrt{\frac{Pr/9 + 1}{18 \overline{f_{c\sigma}} Pr + 1}} \quad (68)$$

The scaling for upstream heating was  $1/2$  in formula (62) for disruptive roughness; the smooth turbulent boundary-layer reduces this interaction;  $\sqrt{1/3} \approx 0.577$  appears correct in the smooth case.

Formula (69) is proposed for smooth-turbulent convection for all  $Pr > 0$ :

$$\overline{Nu}_\sigma = \frac{Nu_0 Re \overline{f_{c\sigma}}}{\sqrt{3}} \sqrt{\frac{Pr/9 + 1}{18 \overline{f_{c\sigma}} Pr + 1}} \sqrt[3]{\frac{Pr}{\Xi \|1, 1/Pr\|_3}} \quad Re \gg \sqrt{3}e \quad (69)$$

Lienhard [20] compares the Gnielinski-White convection formula with local measurements from studies of a variety of fluids with  $0.7 \leq Pr \leq 257$  spanning  $4000 < Re_x < 4.3 \times 10^6$ . The smallest turbulent  $Re_x$  presented was  $\approx 10^5$ . Note that formula (64) is more accurate than Gnielinski-White for turbulent air ( $Pr \approx 0.71$ ) at  $Re_x < 10^5$ .

Figures 16 and 17 show  $\overline{Nu}$  versus  $Pr$  and  $Re$ . The “present work” traces are formula (69). The “Lienhard” traces use formula (70) to numerically average the composition of Gnielinski formula (63) with White formula (12). Note that the averaging of convection  $Nu(Re_x)$  in formula (70) is different from the averaging of skin-friction coefficients presented in Section 17.

$$\overline{Nu}(Re) = \int_{Re_0}^{Re} \frac{Nu(Re_x)}{Re_x} dRe_x \quad (70)$$

Formula (69)  $\overline{Nu}_\sigma$  matches the numerically averaged Gnielinski-White formula within  $\pm 6.5\%$  over the range  $10^5 < Re < 4.3 \times 10^6$  with  $4.0 \leq Pr \leq 257$ . At  $Pr = 0.71$ ,  $\overline{Nu}_\sigma$  matches formula (64)  $\overline{Nu}$  within  $\pm 4\%$  over the range  $10^4 < Re < 4.3 \times 10^6$ .

Over the same ranges, the local convection  $Nu_\sigma = Re_x d\overline{Nu}_\sigma(Re_x)/dRe_x$  matches formula (63) and local formula (64)  $Nu$  within  $\pm 7.5\%$ . Figure 18 shows local  $Nu$  versus  $Re_x$ .

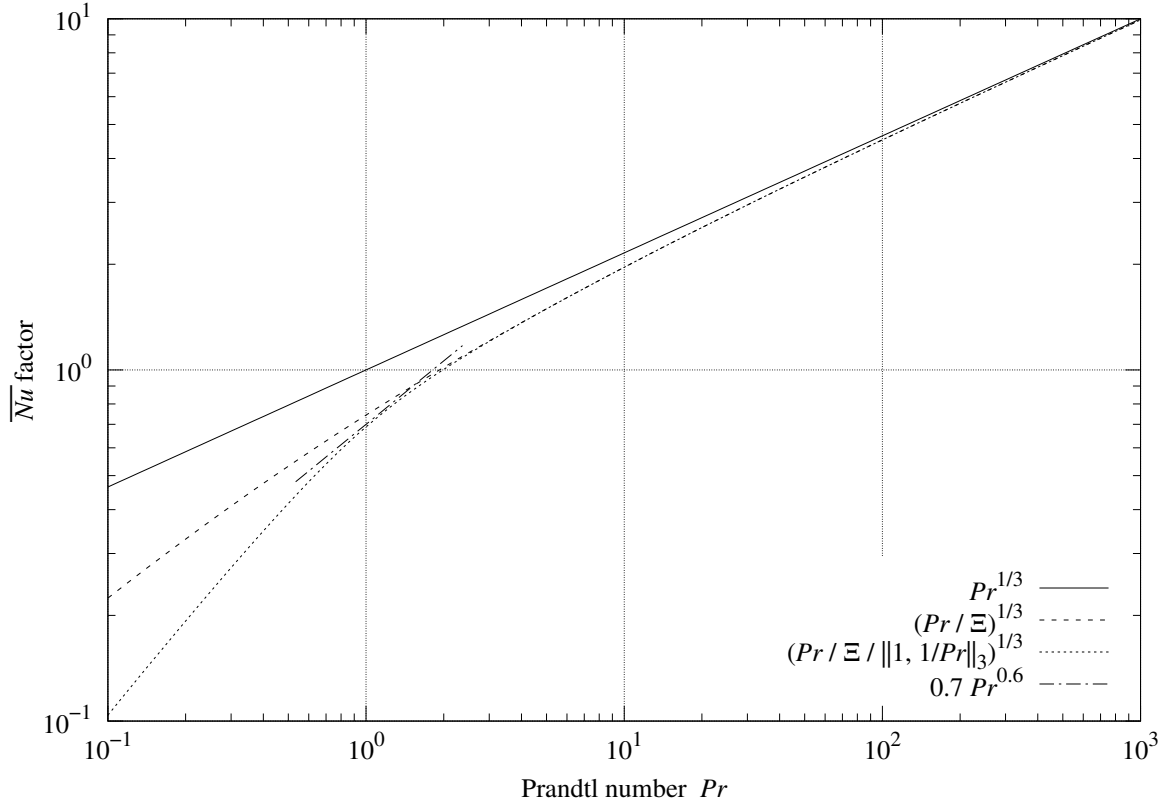


Figure 15 smooth plate  $\overline{Nu}$  dependence on  $Pr$

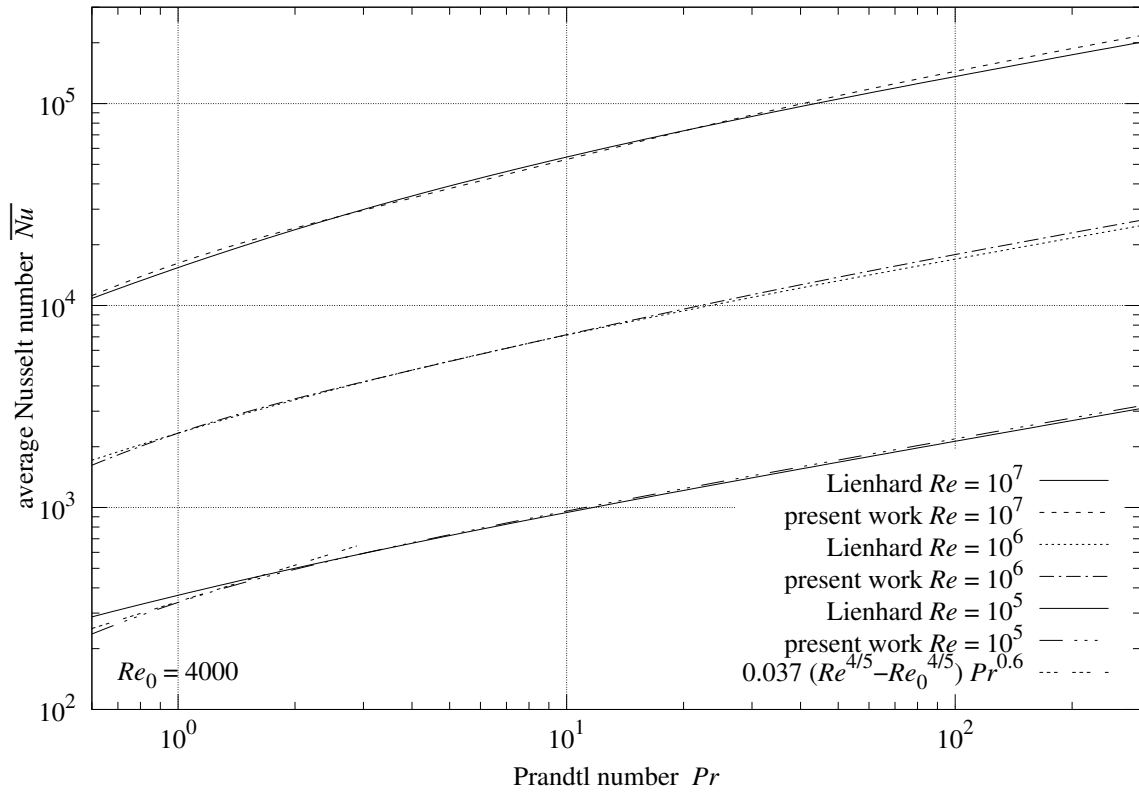


Figure 16 smooth plate average turbulent convection versus  $Pr$

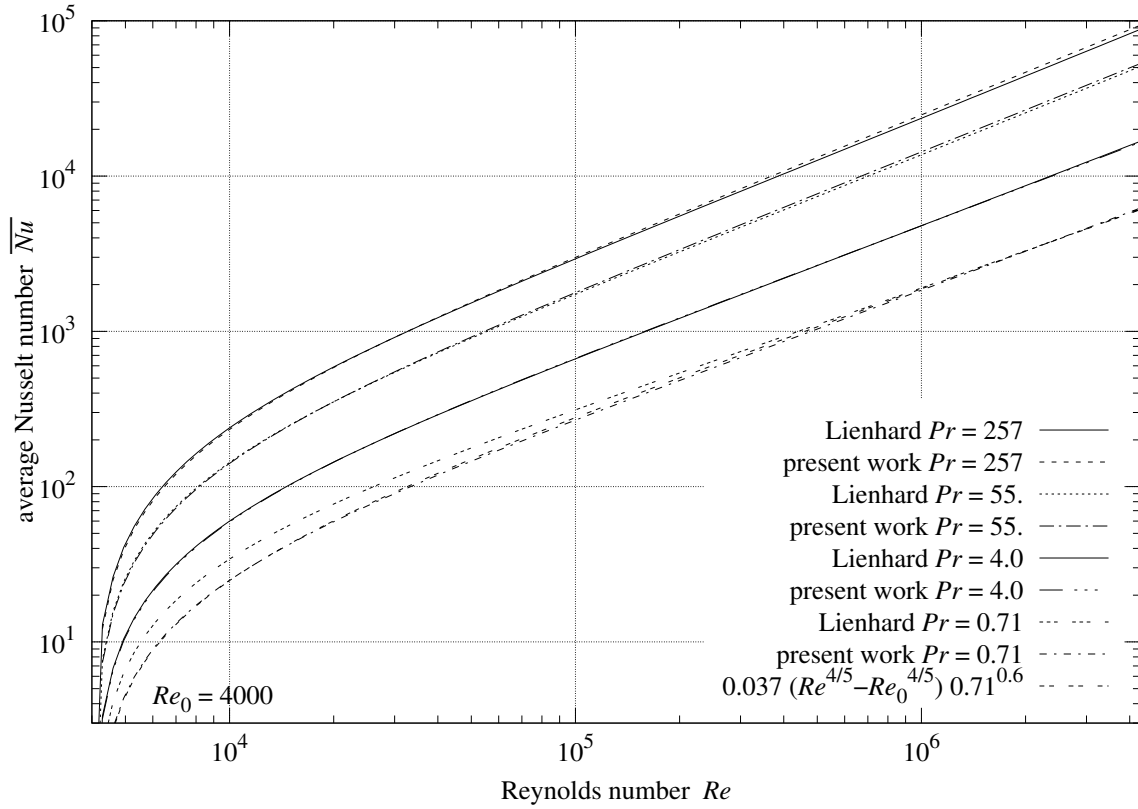


Figure 17 smooth plate average turbulent convection versus  $Re$

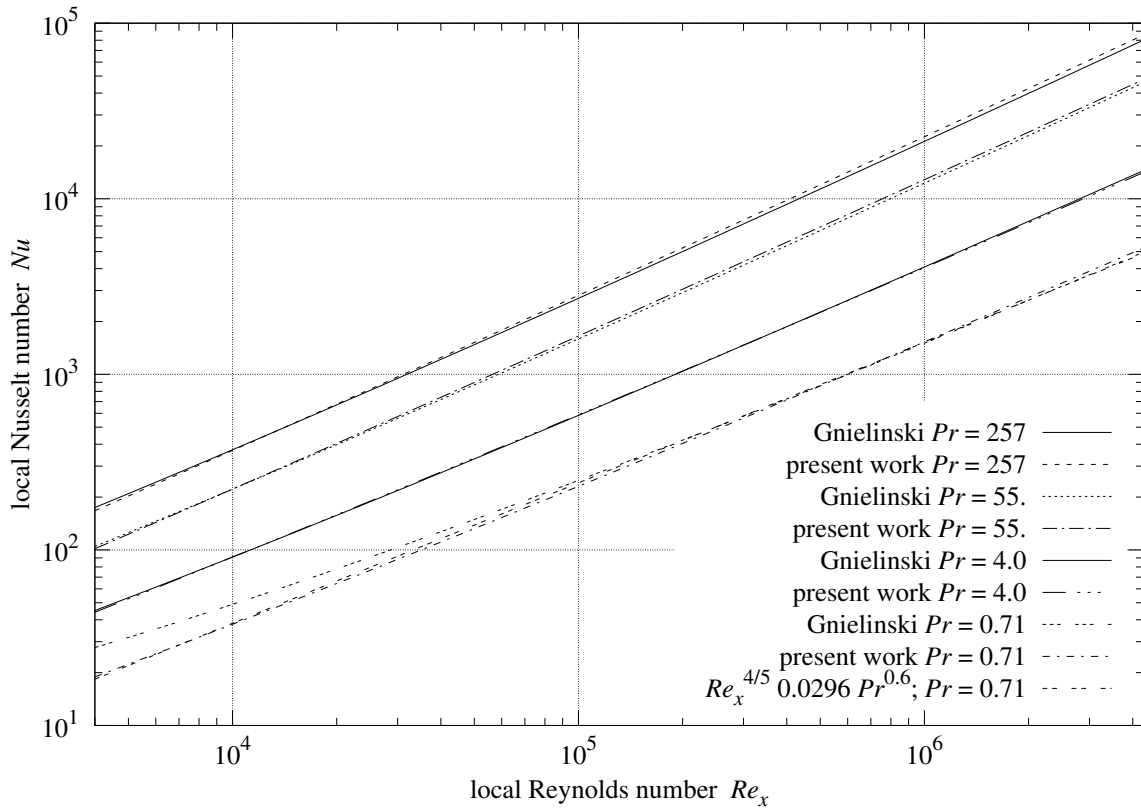


Figure 18 smooth plate local turbulent convection versus  $Re_x$

## 20. Periodic versus self-similar roughness

What can be learned from measurements of skin-friction coefficient and forced-convection from rough plates?

The skin-friction and convection formulas were developed for self-similar roughness. If measurements from plates with self-similar roughness are close to the predictions of skin-friction equation (28) or convection equation (62), then those measurements support the present formulas for self-similar roughness only.

If measurements over a range of  $Re$  values from diverse plates with periodic roughness are close to the present formulas, then it's evidence that the present formulas reflect a physical law of turbulent flow along surface roughness. No self-similar roughness was tested in the present and prior works.

## 21. Fully rough regime

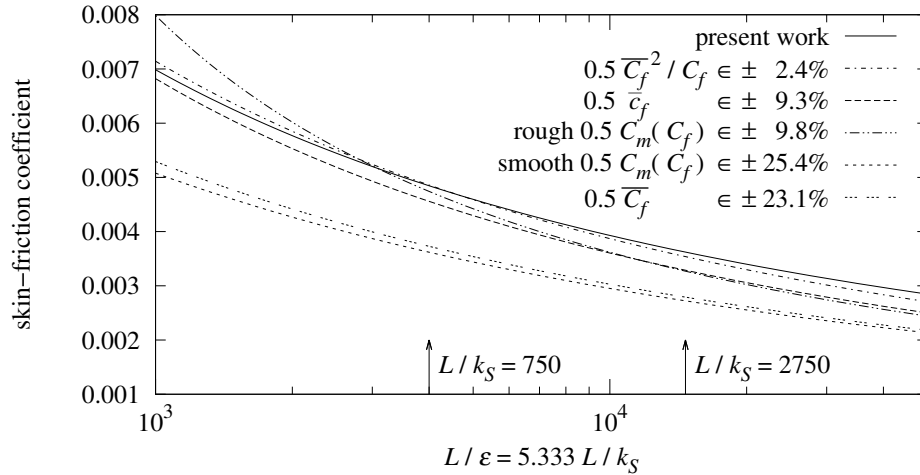


Figure 19 average friction coefficient of sand-roughness

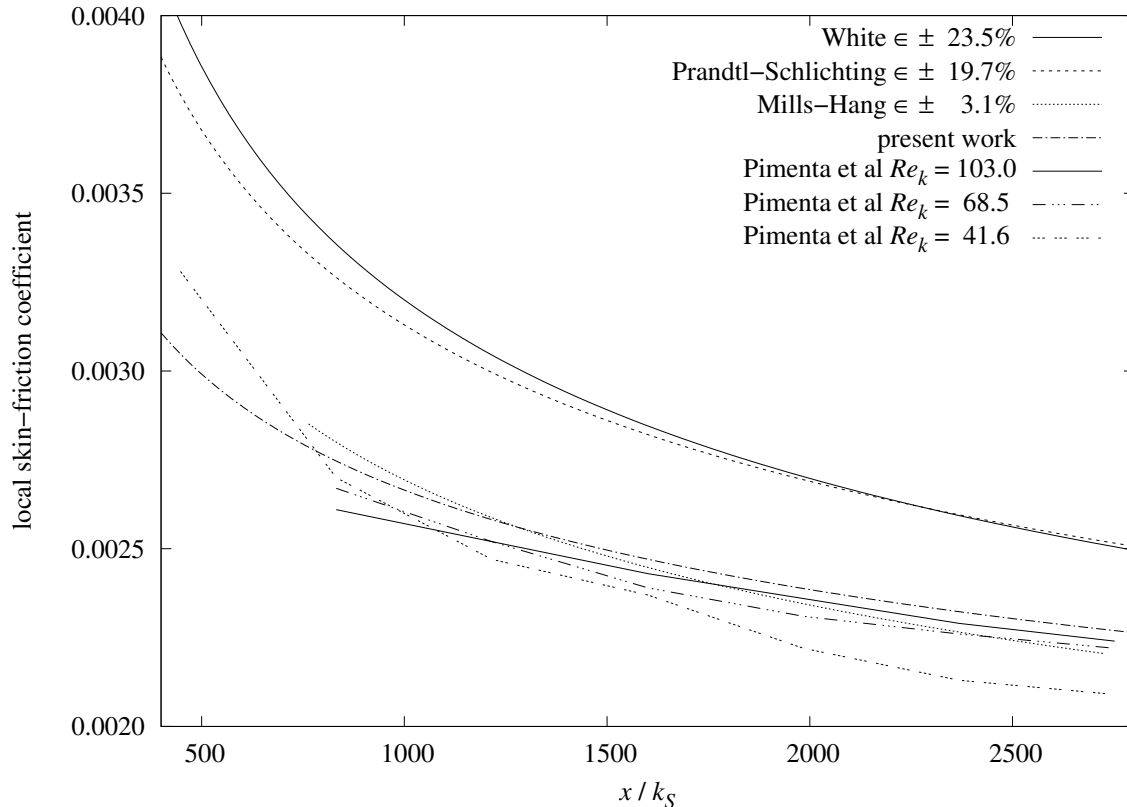


Figure 20 local friction coefficient of sphere-roughened plate

Figure 19 compares average skin-friction formulas in the fully rough regime. To the right of each “ $\pm$ ” is the maximum discrepancy from “present work” equation (28) over the Mills-Hang range  $750 < L/k_S < 2750$ . Starting from the bottom of the Figure 19 key, “0.5  $\overline{C_f}$ ” is the Mills-Hang average formula (10).

The two “0.5  $C_m(C_f)$ ” traces are the Churchill smooth and rough averaging formulas (14) applied to the Mills-Hang local formula (9).

“0.5  $\overline{c_f}$ ” is the Prandtl-Schlichting average formula (8).

“0.5  $\overline{C_f^2}/C_f$ ” is the disrupted boundary-layer averaging formula (57) applied to the Mills-Hang local formula (9); it’s within  $\pm 2.4\%$  of the present work equation (28).

Figure 20 plots the local skin-friction coefficients from White (11), Prandtl-Schlichting (7), Mills-Hang (9), and the present theory (59) in the fully rough regime. The maximum magnitude discrepancy between Mills-Hang and the present theory is 3.1% over the Mills-Hang range  $750 < x/k_S < 2750$ .

The close matches in the fully rough regime, both average and local, support the present theory with measurements from Pimenta et al [5] as modeled by Mills and Hang [6].

## 22. Transitional rough regime

Prandtl and Schlichting describe the boundaries between flow regimes using the “sand-roughness Reynolds number”  $Re_k = u_\tau k_S/\nu \approx 5.333 Re_\varepsilon$  ( $Re_\varepsilon$  from present work equation (29)). They assign the boundaries between the hydraulically smooth, transitional rough, and fully rough regimes at  $Re_k = 7.08$  and  $70.8$ .

Afzal et al [14] (also Schlichting [7]) relates that the turbulent flow inside commercial pipes behaves differently from the flow inside Nikuradse’s sand coated pipes in the transitional rough regime. While the skin-friction coefficients for commercial pipes are monotonically decreasing with increasing  $Re$  on the Moody diagram ( $f_c$  versus  $Re$ ), in the diagram for Nikuradse’s pipes the coefficient trace for each roughness reaches its minimum just to the right of the smooth skin-friction trace, a behavior termed “inflectional”.

The Prandtl-Schlichting plate model inherited the inflectional curve from Nikuradse’s pipes. The coefficients of resistance ( $c_f$  and  $\overline{c_f}$ ) Moody diagrams from Prandtl and Schlichting [1, 7] show  $c_f$  and  $\overline{c_f}$  following a  $-1/5$  slope smooth turbulent trace to a broad 7% dip to the right of the smooth turbulent trace, then rising and leveling out further to the right. An inflectional curve is shown in Figure 21.

For periodic roughness, the present work’s local and average skin-friction formulas (59) and (28) predict no variation in these coefficients for  $Re > Re_\lambda$ .

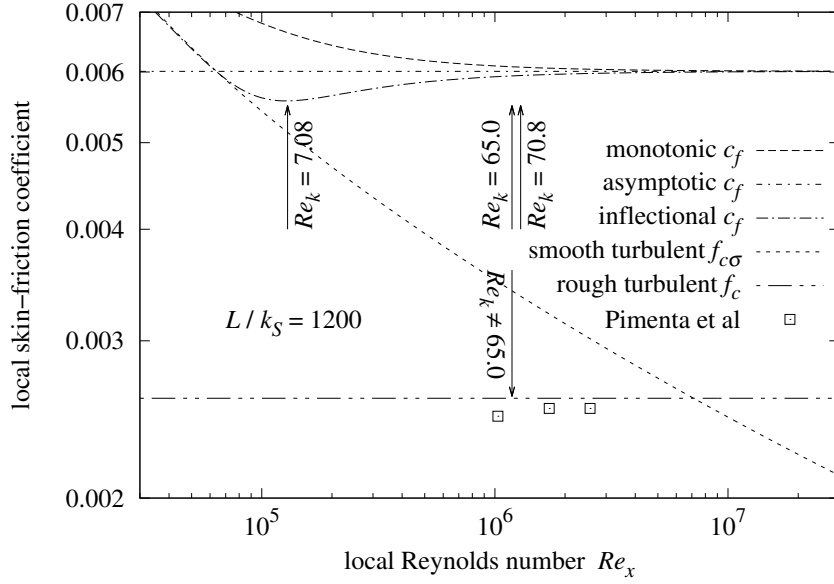
The traces labeled “Pimenta et al” in Figure 20 show the local skin-friction coefficients versus  $x/k_S$  for the Pimenta et al sphere-roughened plate at three rates of flow,  $Re_k = 41.6, 68.5,$  and  $103$ . The averages of these local coefficients from  $750 < x/k_S < 2800$  are  $0.00233, 0.00234,$  and  $0.00241$ , respectively. These averages are within 3.4% of each other. The “Mills-Hang” trace is the fully rough local  $\overline{c_f}/2$ ; its close proximity to the “Pimenta et al” traces indicates a lack of significant behavioral difference between the fully rough and transitional rough regimes. This isn’t definitive, however, because  $Re_k = 41.6$  is moderately close to the  $Re_k = 65.0$  boundary that Pimenta et al assign between the transitional and fully rough regimes.

Figure 21 is a local Moody diagram showing Pimenta et al measurements at  $x/k_S \approx 1200$ , along with regime boundaries and skin-friction coefficients from Prandtl-Schlichting and the present work. The “asymptotic” trace at  $c_f \approx 0.006$  is the Prandtl-Schlichting fully rough skin-friction coefficient for  $x/k_S = 1200$ . The “monotonic” and “inflectional” traces are examples of those types of coefficients at  $x/k_S = 1200$ . The regime boundaries are in the positions expected for the “inflectional” trace.

The measured coefficients are less than half of the Prandtl-Schlichting  $c_f$  coefficient for  $x/k_S \approx 1200$ . Both Mills-Hang and Pimenta et al treat  $c_f/2$  and  $C_f/2$  as the skin-friction coefficients. However,  $Re \approx 1.2 \times 10^6$  (marked  $Re_k \neq 65.0$ ) can’t be the transitional to fully rough boundary for  $c_f/2$  because it and the measurements are to the left of, and less than, the smooth turbulent trace  $f_{c\sigma}$ .

Nor can these measurements be of laminar flow. Laminar flow coefficients would have a larger magnitude slope (versus  $Re_x$ ) than the smooth turbulent curve, but these measurements are nearly at the constant level predicted by the present work.

This is where the pipe-plate analogy fails. Rough turbulent skin-friction coefficients don’t take values less than the smooth turbulent skin-friction coefficient in pipes!



**Figure 21** local  $c_f$  versus  $Re_x$

With  $L_P/\varepsilon < 194$ , formula (40) predicts that the flow along the entire sphere-roughened plate transitions directly from laminar to rough turbulence at  $Re_\lambda \approx 24640$ , but the smallest reported  $Re_x$  for the plate was  $3.8 \times 10^5$ .

Figure 22 plots local  $f_c$  versus  $Re_x$  for the Pimenta et al data-set by  $Re_k$ . Except for the point at  $[3.8 \times 10^5, 0.0033]$ , the measurements are within  $\pm 6\%$  of the present theory.

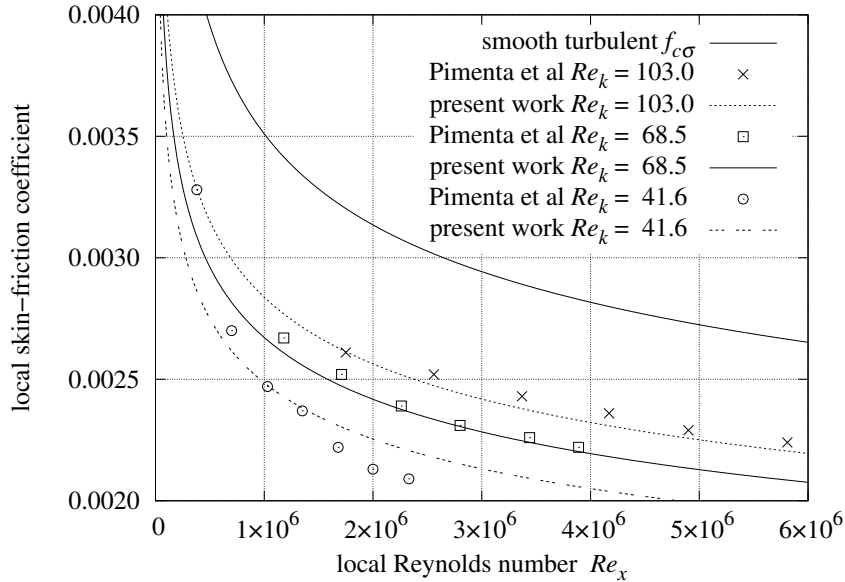


**Figure 22** local  $f_c$  versus  $Re_x$  of sphere-roughened plate

Note that all of these fully rough measurements are significantly less than “smooth turbulent  $f_{c\sigma}$ ”, demonstrating the drag-reduction potential of rough-turbulence.



### 23. Sandpaper

Bergstrom et al [13] has skin-friction coefficient measurements of sandpapers, woven-wire meshes, and perforated sheets attached to flat plates, as well as of the 1.67 m  $\times$  1.16 m flat plate alone. Skin-friction measurements were derived from Pitot probe measurements of air velocity 1.3 m downwind from the leading edge of the plate. The paper [13] gives 5% as the combined measurement uncertainty for the smooth surface friction coefficient, and 9% for rough surfaces.

The measurement tables in [13] include a column for free-stream velocity,  $U_e$ . In order to compute a Reynolds number from  $U_e$ , kinematic viscosity  $\nu = 16 \times 10^{-6}$  m<sup>2</sup>/s was calculated for 20 C air with atmospheric pressure 95 kPa, the average pressure at the University of Saskatchewan.

The points labeled “ $Re_x = 1.3 U_e/\nu$ ” in Figure 23 are all below the “95% smooth  $f_{c\sigma}$ ” trace, placing them outside of the claimed uncertainty of 5%. The “Smith-Walker and Spalding-Chi measurements” are within  $\pm 2\%$  of the “smooth  $f_{c\sigma}$ ” trace (see Figure 14), but lie above “smooth  $f_{c\sigma}$ ”. The Bergstrom et al [13] data is thus in conflict with the Smith-Walker and Spalding-Chi measurements.

If the  $U_e$  column turns out to have already been scaled by 1.3/1.67 (effectively making it  $U_x$ ), then three of the four points are brought within the 5% band, as shown by the points labeled “ $Re_x = L U_e/\nu$ ”. If these measurements were performed using air at -20 C ( $\nu = 12.3 \times 10^{-6}$  m<sup>2</sup>/s), it would also have the effect of bringing three of the four points within the 5% band. The present evaluation continues using  $Re_x = L U_e/\nu$ .

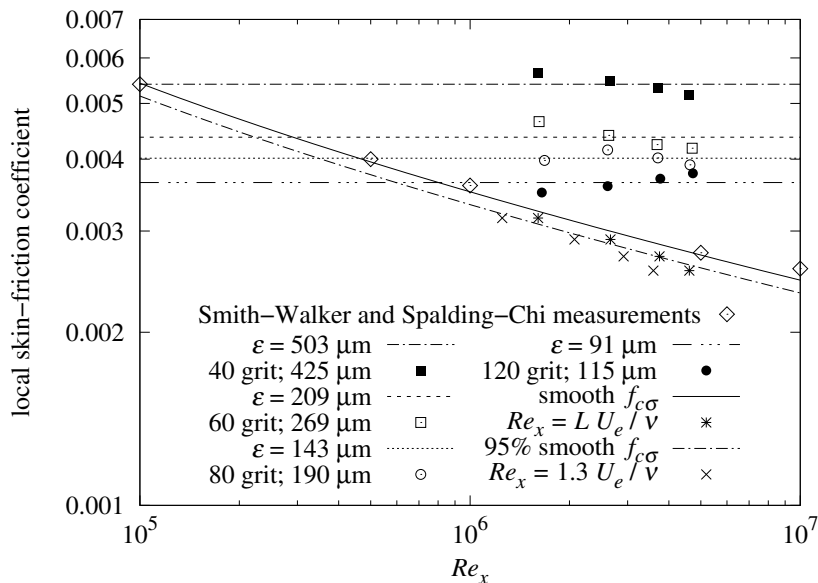


**Figure 23** local  $f_c$  versus  $Re_x$  of sandpaper

Microscopic examination of coarse grades of sandpaper finds mounds of grits and canyons several times the average grit diameter. Sandpaper grit average diameter is standardized, but not the height of roughness; it will vary by manufacturer and lot. The horizontal traces in Figure 23 show that skin-friction coefficients which are independent of  $Re_x$ , as in the present theory, can be within the 9% measurement uncertainty of the data. Note that the RMS height-of-roughness  $\epsilon$  for sandpaper is much larger than  $\epsilon$  for sand-roughness with the same average grit diameter. For example, 40 grit sandpaper has a friction coefficient consistent with  $\epsilon \approx 503 \mu\text{m}$ , while  $k_S = 425 \mu\text{m}$  sand-roughness would have  $\epsilon = k_S/5.333 \approx 80 \mu\text{m}$ .

## 24. Woven wire mesh

Woven wire meshes are specified by wire diameter  $d$  and wire-to-wire spacing  $s$ ; Bergstrom et al [13] calculate mesh openness as  $(s - \sqrt{2}d)^2/s^2$  instead of the  $(s - d)^2/s^2$  used by wire mesh manufacturers. Table 3 shows the dimensions and openness from [13] along with the openness calculated both ways. The WML and WMM meshes have  $(s - \sqrt{2}d)^2/s^2$  values close to those from [13]. The WMS mesh has  $(s - \sqrt{2}d)^2/s^2 \approx 49\%$ , which isn't close to 44%. If the 1.68 mm spacing were instead 1.48 mm, then it has  $(s - \sqrt{2}d)^2/s^2 \approx 44\%$ , but has significantly less friction coefficient than the WMS measurements in Figure 24. If the 0.36 mm wire diameter was instead 0.56 mm, then it has conventional openness  $(s - d)^2/s^2 \approx 44\%$ , and is nearly coincident with the WMM trace and data.

wire diameter $d$	center spacing $s$	$(s - d)^2/s^2$	$(s - \sqrt{2}d)^2/s^2$	openness in [13]
1.04 mm	3.68 mm	52%	36%	35% WML
0.58 mm	1.77 mm	45%	29%	30% WMM
0.36 mm	1.68 mm	62%	49%	<u>44%</u> WMS
0.36 mm	1.48 mm	58%	<u>44%</u>	
0.56 mm	1.68 mm	<u>44%</u>	28%	

**Table 3** wire mesh dimensions

There are periodic gaps between the wires and the plate; so the mesh-plate combination isn't strictly a roughness. Ignoring the gaps, the RMS height-of-roughness  $\varepsilon$  would be:

$$z(x, y) = \sqrt{\frac{d^2}{4} - x^2} + d - \frac{d}{2} \cos \frac{\pi y}{s} \quad \bar{z} = \frac{4}{s^2} \int_{d/2}^s \int_0^{d/2} z(x, y) dx dy \quad (71)$$

$$\varepsilon = \frac{4}{s^2} \int_{d/2}^s \int_0^{d/2} |z(x, y) - \bar{z}|^2 dx dy + \frac{(s - d)^2 \bar{z}^2}{s^2}$$

The periodic gaps between the wire and plate provide for more turbulence from the flow. As a first-order approximation, the height-of-roughness can be scaled by the square root of the ratio of the side area including the gap to the side area excluding the gap, an increase of  $\approx 26\%$ :

$$\varepsilon' = \varepsilon \sqrt{\frac{12s + \pi d}{8s}} \quad (72)$$

Figure 24 trace “unscaled 1.04, 3.68 mm” shows the skin-friction of the WML mesh without this scaling.

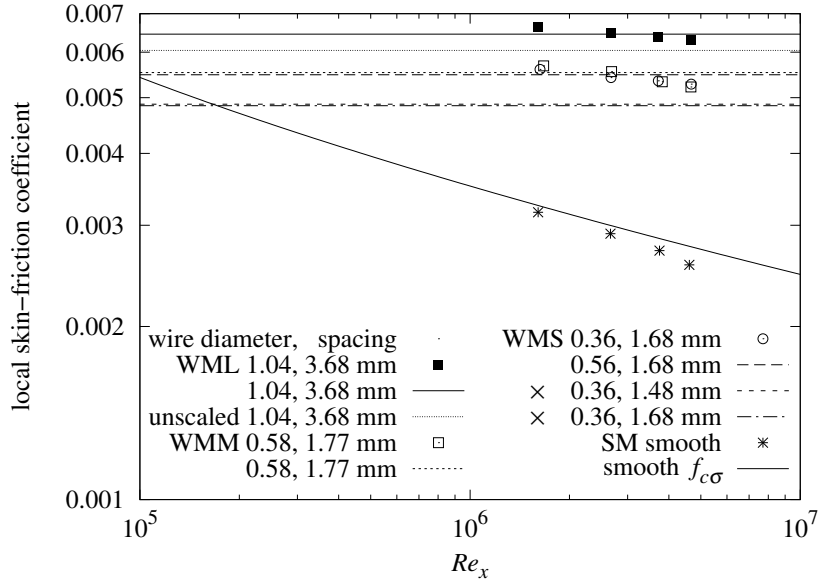


**Figure 24** local  $f_c$  versus  $Re_x$  of woven wire mesh

With scaled  $\varepsilon$ , the WML and WMM measurements match the present theory well within the  $\pm 9\%$  measurement uncertainty. The WMS measurements don't match unless a hypothesized single digit misprint in [13] is corrected, changing the wire diameter from 0.036 mm to 0.056 mm.

## 25. Perforated sheet

Table 4 checks the openness of the perforated sheets which Bergstrom et al [13] tested. It finds that the holes were hexagonally arrayed, and reveals a discrepancy in the text of the paper; the PS sheet’s calculated openness is half of the paper’s 22%. There are two single digit changes which would result in hexagonal openness near 22%: hole diameter  $d = 1.7$  mm or center spacing  $s = 2.4$  mm.

The North American suppliers of perforated sheet metal generally specify the hole and center spacing dimensions in terms of 1/64 of an inch. Table 4 provides the dimensions in both millimeters and fractions of an inch.  $d = 3/64$  with  $s = 6/64$  is a standard size;  $d = 4.3/64$  with  $s = 8.6/64$  is not. Therefore, it seems likely that the 3.40 mm spacing in the PS row should have been 2.40 mm.

hole diameter	center spacing	square openness	hexagonal openness	openness in [13]	
2.0 mm $\approx 5/64$	2.81 mm $\approx 7/64$	40%	46%	45%	PL
1.6 mm $\approx 4/64$	2.43 mm $\approx 6/64$	34%	40%	41%	PM
1.2 mm $\approx 3/64$	3.40 mm $\approx 8.6/64$	10%	11%	<u>22%</u>	PS
1.7 mm $\approx 4.3/64$	3.40 mm $\approx 8.6/64$	19%	<u>23%</u>		
1.2 mm $\approx 3/64$	2.40 mm $\approx 6/64$	19%	<u>23%</u>		

**Table 4** perforated sheet openness

Table 5 shows the dimensions and metrics of the perforated sheets when laid on the flat plate. In the formulas of Section 14,  $[4L_*] = d$  and  $L_P = s$ .

hole diameter	center spacing	thickness	openness	$d^2/s^2$	$\epsilon$	$Re_w$
2.0 mm	2.81 mm	0.90 mm	46% PL	0.507	0.449 mm	$2.06 \times 10^6$
1.6 mm	2.43 mm	0.90 mm	40% PM	0.434	0.441 mm	$4.17 \times 10^6$
1.2 mm	2.40 mm	0.76 mm	23% PS	0.250	0.318 mm	$2.80 \times 10^6$

**Table 5** perforated sheet dimensions

For PL,  $[4L_*]^2/L_P^2 \approx 0.507$  from Table 5 is larger than 1/2; flow will be rough turbulent. The “ $f_c(2898) = 0.0052$ ” trace in Figure 25 shows the predicted local skin-friction coefficient’s close proximity to the PL measurements. The “ $\times 2.00$  mm, 2.81 mm, 0.90 mm” trace with transition at “PL $\times$ ” shows the behavior predicted if  $[4L_*]^2/L_P^2 < 1/2$  had been the case.

Sheets PM and PS have  $0 \leq [4L_*]^2/L_P^2 < 1/2$ . At formula (48)  $Re_w$ , which is marked by down arrows in Figure 25, their local coefficient switches from mix formula (50) to smooth turbulence from formula (52).

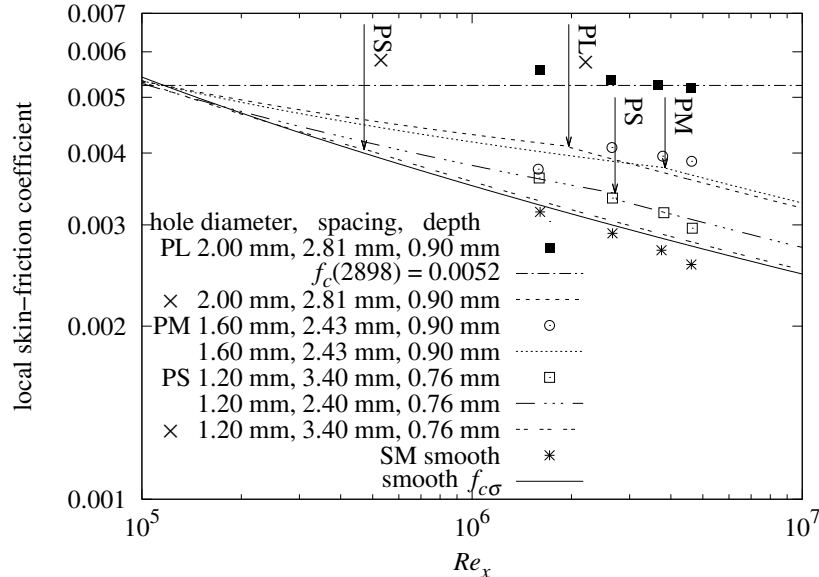


**Figure 25** local  $f_c$  versus  $Re_x$  of perforated sheet

PL and PM measurements match the present theory within the  $\pm 9\%$  measurement uncertainty. The PS measurements don’t match unless a hypothesized single digit misprint in [13] is corrected, changing the PS hole spacing from 3.4 mm to 2.4 mm. The “PS $\times$ ” trace shows the behavior predicted of the original PS.

## 26. Convection measurements

The present apparatus [24] combined an open intake wind-tunnel and an aluminum plate containing a heater and temperature transducers. This combination was able to measure average convection in air at flow rates  $2300 < Re < 90000$ .

The periodic bi-level plate surface was milled to have (676) square  $8.5 \text{ mm} \times 8.5 \text{ mm} \times 6 \text{ mm}$  posts spaced on  $11.7 \text{ mm}$  centers over the  $0.305 \text{ m}$  square plate. The area of the top of each post was  $0.722 \text{ cm}^2$ , 56% of its  $1.37 \text{ cm}^2$  cell. The RMS height-of-roughness was  $3 \text{ mm}$ .

The operating methodology was unusual in that it didn't wait for temperatures to stabilize before taking measurements. Instead, it captured a time sequence of all measured quantities and inferred the convection from that dynamic sequence.

Section 31 describes the apparatus and measurement methodology in greater detail.

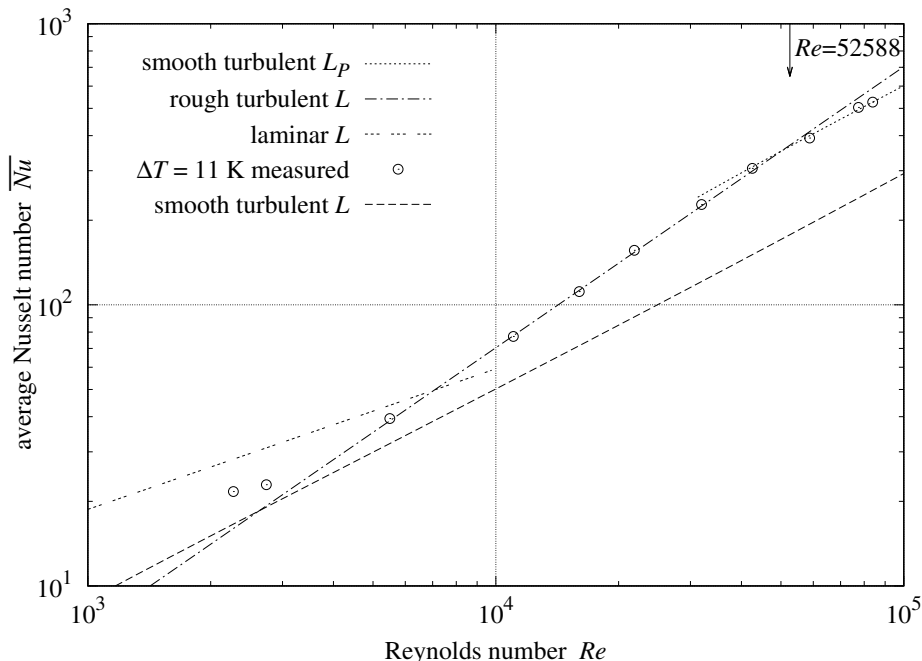


**Figure 26** convection from bi-level plate;  $L/\varepsilon = 305/3$

The two edges of the plate roughness parallel to the flow also contribute to forced convection, increasing the effective width of the bi-level plate by  $\sqrt{2}\varepsilon$  (1.4%). Applying the present convection formula (62) to the bi-level plate geometry (with the 1.4% correction) yields:

$$\overline{Nu} = 0.0079 Re Pr^{1/3} \quad (73)$$

In Figure 26, the points labeled “ $\Delta T = 11 \text{ K}$  measured” are the  $\overline{Nu}$  values calculated from measurements with the plate averaging  $11 \text{ K}$  warmer than the ambient air. At  $Re < 5000$ , the natural convection component dominates the mixed convection. The “rough turbulent  $L$ ” trace in Figure 26 is equation (73); it matches the “measured” points  $\pm 2.5\%$  for  $5000 < Re < 50000$ . At  $Re > 50000$  the “smooth turbulent  $L_P$ ” trace (having slope  $4/5$ ) shows that convection is from a smooth turbulent flow, but with a shorter characteristic-length than the “smooth turbulent  $L$ ” trace. Equation (46) calculates that this transition is at  $Re_i \approx 52588$ , which is marked with a down arrow in Figure 26.

With  $L_P/\varepsilon < 194$ , formula (40) predicts that the flow along the entire bi-level plate transitions directly from laminar to rough turbulence at  $Re_\lambda \approx 175$ , which is too slow to test in the present apparatus.

The periodic bi-level plate behaving compatibly with formula (62), which was derived from an analysis of self-similar roughness, supports the claim that formulas (28) and (62) are intrinsic to turbulent flow along isotropic roughness, and not limited to self-similar roughness.

## 27. Discussion

Rather than trying to tease rough turbulence from a nearly smooth surface, the present work starts its analysis with roughness which is much thicker than smooth boundary layers. Recapitulating the development:

- Self-similar roughness repeatedly disrupts emerging boundary-layers along a plate.
- Self-similar roughness has a constant characteristic-length to RMS height-of-roughness ratio  $L/\varepsilon \gg 1$  at a succession of scales converging to zero. This leads to friction velocity  $u_\tau = u/[\sqrt{3} \ln(L/\varepsilon)]$ .
- Plate surfaces with isotropic self-similar roughness have skin-friction coefficient:  $\overline{f_c} = [1/3] \ln^{-2}(L/\varepsilon)$ .
- Consideration of roughness Reynolds number  $Re_\varepsilon = 1$  leads to a formula for the turbulent average skin-friction coefficient for smooth plates:  $\overline{f_{c\sigma}} = [\sqrt[3]{2}/3] [W_0(Re/\sqrt{3}) - 1]^{-2}$ . This formula matches measurements from Smith and Walker [18] and Spalding and Chi [19] with 0.75% RMSRE.
- $j_P = \sqrt{j^2 + k^2}$ , where  $j, k$  are the indexes of the  $w \times w$  Fourier transform coefficient  $X_{j,k}$  with the largest amplitude. Self-similar roughness has  $j_P = 1$ ;  $j_P \gg 1$  is periodic roughness with period  $L_P = L/j_P$ .
- A periodic surface is isotropic if its  $j_P = L/L_P$  varies no more than  $\pm w/32$  through its full rotation.
- The transition from laminar or smooth turbulent flow to rough turbulent flow along a plate with isotropic periodic roughness should occur when  $\varepsilon$  exceeds the larger of the smooth turbulent or laminar momentum thicknesses of a smooth plate at  $x = L_P$ . Available data lacked  $Re$  small enough to verify the actual transitions. However, the data shows that the transitions must be at much smaller  $Re$  than the smooth-rough skin-friction intercept, which bounds the transition in pipes.
- Flow along flat-peak roughness can transition from rough to smooth turbulent flow with increasing  $Re$ . Of the four isotropic periodic flat-peak roughness configurations, the three for which measurements were available were successfully modeled and tested.
- Rough turbulent convection is:  $\overline{Nu} = Re Pr^{1/3}/[6 \ln^2(L/\varepsilon)]$ . Bi-level plate experiments by the author match this formula  $\pm 2.5\%$  for  $5000 < Re < 50000$ .
- The similarity of forced convection to natural convection from a vertical plate leads to a formula for smooth turbulent average forced convection. This formula matches the (averaged) turbulent formula from Lienhard [20] within  $\pm 6.5\%$  over  $10^5 < Re < 4.3 \times 10^6$  with  $4.0 \leq Pr \leq 257$ .
- Experiments with the isotropic periodic roughness of bi-level, sphere-roughened, mesh-covered, and perforated plates find that convection and skin-friction coefficients are close to the present theory formulas with  $Re$  as small as 5000 and as large as  $5 \times 10^6$ .

In a departure from prior works, the present theory does not admit an intermediate flow regime between smooth and rough turbulence for isobaric plates. Section 16 models rough and smooth turbulence occurring simultaneously along distinct regions of a plate when its peaks of roughness are co-planar flats. This phenomenon is controlled by the peaks; the woven wire meshes of Section 24 had flat co-planar valleys, not peaks; they were successfully modeled as producing rough turbulence only.

In order for flat-peaked roughness to be able to sustain smooth turbulent flow, the flat peaks must have sufficient length to build boundary layers to bridge the gaps. For isotropic periodic roughness,  $4L_*$  characterizes the (island or well) convex region and  $L_P$  is the characteristic-length of the cell.

In Figure 25 (perforated sheets), the PL measurements with  $[4L_*]^2/L_P^2 \approx 0.507$  show rough turbulence, while the PM measurements with  $[4L_*]^2/L_P^2 \approx 0.434$  are a mixture of rough and smooth turbulence (from distinct areas of the plate). The square post bi-level plate of Section 26 with  $[4L_*]^2/L_P^2 \approx 0.556$ , produces smooth-turbulence when  $Re_x > Re_i$ . Together, these suggested that the criterion for the appearance of smooth-turbulent flow is  $[4L_*]^2/L_P^2 > 0.5$  for flat-peaked islands and  $[4L_*]^2/L_P^2 < 0.5$  for flat-peaked wells.

Note that use of the peak area fraction  $1 - \Omega$  instead of  $[4L_*]^2/L_P^2$  wouldn't separate (at 0.5) the PL plate  $1 - \Omega \approx 0.541$  from the PM plate  $1 - \Omega \approx 0.607$ , which have markedly different behaviors in Figure 25.

The Colburn [25] analogies relate friction factors to forced convective heat transfer. For laminar flow:

$$\overline{Nu} = \frac{\overline{f_c}}{2} Re Pr^{1/3} \quad (74)$$

Note that combining equation (74) with rough  $\overline{f_c}$  equation (28) results in  $\overline{Nu} = Re Pr^{1/3}/[6 \ln^2(L/\varepsilon)]$ , which is the same as rough turbulent convection equation (62).

Equation (74) is the original (1933) form of the Chilton-Colburn analogy. Lienhard [20] demonstrates that the analogy's  $Re$  and  $Pr$  exponents aren't correct for smooth turbulent flow in all fluids. In particular, the  $Pr$  exponent should be 0.6 in gasses. The present theory matches rough turbulent convection on the present apparatus within its  $\pm 2.5\%$  root-sum-squared (RSS) measurement uncertainty using  $Pr^{1/3}$ . With  $Pr = 0.71$  (air),  $Pr^{0.6} \approx 0.814$  is nearly 9% smaller than  $Pr^{1/3} \approx 0.892$ , a deviation greater than 3 times the measurement uncertainty. This is further evidence of the difference in character between rough and smooth turbulence along external plates.

If an intermediate isobaric flow regime is needed for other plate roughness geometries, it will pose an interesting challenge for forced convection, whose dependence on  $Pr$  is radically different between smooth and rough turbulence.

The combination of periodicity and isotropy make possible the modeling of a large class of plate roughness geometries (many of practical interest) with few parameters:  $L$ ,  $\varepsilon$ ,  $L_P$ , and additionally,  $L_*$  and  $\Omega$  when peaks are flat.

## 28. Conclusions

- For a flat, smooth plate which is inducing turbulence in a steady flow of strength  $Re$ , the average skin-friction coefficient and forced convection formulas are:

$$\overline{f_{c\sigma}} = \frac{\sqrt[3]{2}/3}{[W_0(Re/\sqrt{3}) - 1]^2} \quad \overline{Nu}_\sigma = \frac{Nu_0 Re \overline{f_{c\sigma}}}{\sqrt{3}} \sqrt{\frac{Pr/9+1}{18 \overline{f_{c\sigma}} Pr + 1}} \sqrt[3]{\frac{Pr}{\Xi \|1, 1/Pr\|_3}}$$

where  $W_0$  is the principal branch of the Lambert W function, the inverse of  $\vartheta = \varphi \exp(\varphi)$ , and:

$$Nu_0 = \frac{16}{\pi^2 \sqrt[4]{2}} \quad \Xi = \left\| 1, \frac{0.5}{Pr} \right\|_{\sqrt{1/3}} \quad \|\varphi, \vartheta\|_p = (|\varphi|^p + |\vartheta|^p)^{1/p} \quad Re \gg \sqrt{3}e$$

- For a plate surface with isotropic periodic roughness having RMS height-of-roughness  $\varepsilon > 0$ , which is inducing rough turbulence in a steady flow of strength  $Re$ , the average skin-friction coefficient and forced convection formulas are:

$$\overline{f_c} = \frac{1}{3 \ln^2(L/\varepsilon)} \quad \overline{Nu} = \frac{Re Pr^{1/3}}{6 \ln^2(L/\varepsilon)} \quad \frac{L}{\varepsilon} \gg 1$$

- The roughness spatial period  $L_P = L/\sqrt{j^2 + k^2} \ll L$ , where  $0 \leq j \leq w/2$  and  $0 \leq k \leq w/2$  are the indexes of the  $w \times w$  discrete spatial Fourier transform coefficient  $X_{j,k}$  having the largest amplitude.
- A periodic surface is isotropic if its  $j_P = L/L_P$  varies no more than  $\pm w/32$  through its full rotation.
- For isotropic periodic roughness with period  $L_P \ll L$ , the flow along the entire plate should transition from laminar to rough turbulence at  $Re \approx Re_\lambda$  if  $Re_\sigma < Re_\lambda$ , or from laminar to smooth turbulence at  $Re \approx Re_\lambda$ , and to rough turbulence at  $Re \approx Re_\sigma$  when  $Re_\sigma > Re_\lambda$ .

$$Re_\lambda = \left[ \frac{0.664}{\varepsilon} \right]^2 L_P L \quad Re_\sigma = \frac{\sqrt{3} L}{3^3 \varepsilon} \exp \frac{L_P}{3^3 \varepsilon}$$

- For isotropic periodic roughness whose peaks are all co-planar flat areas, flow can transition from rough to smooth turbulent as  $Re$  increases. Formulas for the  $Re_x$  thresholds, convection, and skin-friction coefficients were developed and found to be consistent with measurements from Bergstrom, Akinlade, and Tachie, and from experiments conducted by the present author.

## 29. Nomenclature

	$A$	= rough plate area (m <sup>2</sup> )
	$c_f, \overline{c_f}$	= local, average skin-friction coefficient Prandtl-Schlichting [1]
	$C_f/2, \overline{C_f}/2$	= local, average skin-friction coefficient Mills-Hang [6]
	$C_f/2$	= local skin-friction coefficient Pimenta et al [5]
	$C_m/2$	= mean (average) skin-friction coefficient Churchill [9]
	$f_c, \overline{f_c}$	= local, average skin-friction coefficient present work
	$G(t, w)$	= Gray-code self-similar ramp-permutation
	$j_P$	= period index, the index of largest $ X_j $ or $ X_{j,k} $
	$k_S$	= sand-roughness (m)
	$L$	= plate characteristic-length (m)
	$L_P$	= roughness spatial period (m)
	$L_*$	= ratio of flat-peak convex region area to its perimeter (m)
	$n$	= branching factor of profile roughness function
	$Nu, \overline{Nu}$	= local, average Nusselt number (convection)
	$Pr$	= Prandtl number of fluid
	$q = \log_2 w$	= positive integer
	$Re$	= Reynolds number of flow parallel to the plate
	$Re_i, Re_w$	= $Re_x$ rough-to-smooth turbulence threshold
	$Re_\lambda, Re_\sigma$	= laminar, smooth turbulent $Re$ upper-bound
	$Re_\varepsilon = u_\tau \varepsilon / \nu, Re_k = u_\tau k_S / \nu$	= roughness, sand-roughness Reynolds number
	$Re_x = x Re / L$	= local Reynolds number
	$Re_0$	= $Re_x$ integration lower bound
	$t$	= integer
	$u$	= bulk fluid velocity (m/s)
	$u_\tau$	= friction velocity (m/s)
	$w = 2^q$	= integer power of two
	$W(t, w)$	= wiggliest integer self-similar ramp-permutation
	$W_0$	= principal branch of the Lambert W function
	$x$	= distance from leading edge of plate (m)
	$X_j, X_{j,k}$	= discrete Fourier transform coefficient
	$Y(t, w)$	= integer self-similar ramp-permutation
	$z$	= roughness function (m)
	$\bar{z}$	= mean elevation of roughness function (m)
	$Z$	= roughness random variable (m)

## Greek Symbols

	$\delta_2$	= momentum thickness of boundary-layer flow (m)
	$\delta_{2\lambda}, \delta_{2\sigma}$	= laminar, smooth turbulence momentum thickness (m)
	$\varepsilon, \varepsilon$	= profile, surface RMS height-of-roughness (m)
	$\varepsilon_{pv}$	= peak to valley height-of-roughness (m)
	$\nu$	= fluid kinematic viscosity (m <sup>2</sup> /s)
	$\Omega$	= ratio of non flat-peak area to cell area (m <sup>2</sup> /m <sup>2</sup> )
	$\rho$	= fluid density (kg/m <sup>3</sup> )
	$\tau, \tau_2$	= fluid shear stress (N/m <sup>2</sup> )
	$\varsigma$	= peak elevation of roughness (m)
	$\varphi, \vartheta$	= mathematical variables

## Acknowledgments

The idea of self-similar roughness grew from a discussion with Nina Koch about turbulence self-similarity. Thanks to John Cox and Doug Ruuska for machining the bi-level plate. Thanks to Martin Jaffer for critiques and insights. Thanks to anonymous reviewers for their useful suggestions.

## 30. References

- [1] L. Prandtl and H. Schlichting. *The Resistance Law for Rough Plates*. Translation (David W. Taylor Model Basin). Navy Department, the David W. Taylor Model Basin, 1934. Translated 1955 by P.S. Granville.
- [2] J. Nikuradse. Laws of flow in rough pipes. *VDI Forschungsheft*, page 361, 1933. Translated 1937 by A. A. Brielmaier.
- [3] H Schlichting. Experimental investigation of the problem of surface roughness. Technical Report TM 823, NACA, Washington, DC, 1937.
- [4] F. R. Hama. Boundary layer characteristics for smooth and rough surfaces. *Trans. Soc. Nav. Arch. Marine Engrs.*, 62:333–358, 1954.
- [5] M. M. Pimenta, R. J. Moffat, and W. M. Kays. *The Turbulent Boundary Layer: An Experimental Study of the Transport of Momentum and Heat with the Effect of Roughness*. Department of Mechanical Engineering, Stanford University, 1975.
- [6] A. F. Mills and Xu Hang. On the skin friction coefficient for a fully rough flat plate. *J. Fluids Eng*, 105(3):364–365, 1983.
- [7] Hermann Schlichting, Klaus Gersten, Egon Collaborateur. Krause, Herbert Collaborateur. Oertel, and Katherine Mayes. *Boundary-layer theory*. Springer, Berlin, Heidelberg, Paris, 2000. Corrected printing 2003.
- [8] Frank White. *Viscous Fluid Flow, 3rd Edition*. McGraw-Hill, 2006.
- [9] Stuart W. Churchill. Theoretically based expressions in closed form for the local and mean coefficients of skin friction in fully turbulent flow along smooth and rough plates. *International Journal of Heat and Fluid Flow*, 14(3):231 – 239, 1993.
- [10] C. F. Colebrook. Turbulent flow in pipes, with particular reference to the transition region between the smooth and rough pipe laws. *Journal of the Institution of Civil Engineers*, 11(4):133–156, 1939.
- [11] Javier Jiménez. Turbulent flows over rough walls. *Annual Review of Fluid Mechanics*, 36(1):173–196, 2004.
- [12] Mark F. Tachie, D. J. Bergstrom, Ram Balachandar, and Shyam Ramachandran. Skin Friction Correlation in Open Channel Boundary Layers . *Journal of Fluids Engineering*, 123(4):953–956, 05 2001.
- [13] D. J. Bergstrom, O. G. Akinlade, and M. F. Tachie. Skin Friction Correlation for Smooth and Rough Wall Turbulent Boundary Layers. *Journal of Fluids Engineering*, 127(6):1146–1153, 04 2005.
- [14] Noor Afzal, Abu Seena, and A. Bushra. Turbulent flow in a machine honed rough pipe for large reynolds numbers: General roughness scaling laws. *Journal of Hydro-environment Research*, 7(1):81–90, 2013.
- [15] Karen A Flack, Michael P Schultz, Julio M Barros, and Yechan C Kim. Skin-friction behavior in the transitionally-rough regime. *International Journal of Heat and Fluid Flow*, 61:21–30, 2016.
- [16] J. H. Lienhard, IV and J. H. Lienhard, V. *A Heat Transfer Textbook*. Phlogiston Press, Cambridge, MA, 5th edition, August 2020. Version 5.10.
- [17] Mitchell G. Newberry and Van M. Savage. Self-similar processes follow a power law in discrete logarithmic space. *Phys. Rev. Lett.*, 122:158303, Apr 2019.
- [18] D. W. Smith and J. D. Walker. Skin friction measurements in incompressible flow. Technical Report R-26, NASA, Washington, DC, 1959.
- [19] D. B. Spalding and S. W. Chi. The drag of a compressible turbulent boundary layer on a smooth flat plate with and without heat transfer. *Journal of Fluid Mechanics*, 18(1):117143, 1964.



- [20] V Lienhard, John H. Heat Transfer in Flat-Plate Boundary Layers: A Correlation for Laminar, Transitional, and Turbulent Flow. *Journal of Heat Transfer*, 142(6), 04 2020. 061805.
- [21] RJ Goldstein, EM Sparrow, and DC Jones. Natural convection mass transfer adjacent to horizontal plates. *International Journal of Heat and Mass Transfer*, 16(5):1025–1035, 1973.
- [22] JR Lloyd and WR Moran. Natural convection adjacent to horizontal surface of various planforms. *Journal of Heat Transfer*, 96(4):443–447, 1974.
- [23] Aubrey Jaffer. Thermodynamic basis for natural convection from an isothermal plate, 2021. <http://people.csail.mit.edu/jaffer/convect/thermo.pdf>.
- [24] Aubrey Jaffer. Convection measurement apparatus and methodology, 2021. <http://people.csail.mit.edu/jaffer/convect/measure.pdf>.
- [25] Allan P. Colburn. A method of correlating forced convection heat-transfer data and a comparison with fluid friction. *International Journal of Heat and Mass Transfer*, 7(12):1359 – 1384, 1964.
- [26] Rice R.W. Emittance factors for infrared thermometers used for wood products. *Wood and Fiber Science*, 36:520–526, 2004.
- [27] R.B. Abernethy, R.P. Benedict, and R.B. Dowdell. Asme measurement uncertainty. *ASME. J. Fluids Eng.*, 107(2):161–164, 1985.

### 31. Appendix: convection measurement apparatus and methodology

This section excerpts from Jaffer [24], which describes the apparatus and methodology in great detail.

Starting in 2015 an apparatus was constructed to measure total (not local) forced convection in air from a heated 305 mm square plate with precisely 3 mm of roughness.

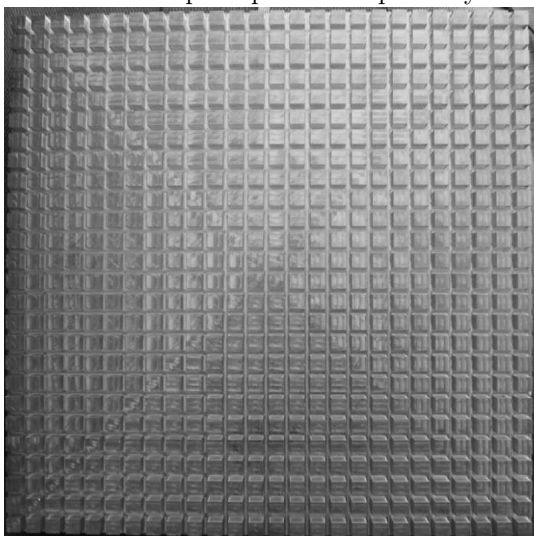


**Figure 27** rough surface of plate



**Figure 28** cross-section of plate

Figure 27 shows the rough surface of the 30.5 cm × 30.5 cm test plate. Machined from MIC-6 aluminum to keep its emissivity low, the reflective surface is composed of (676) 8.5 mm × 8.5 mm × 6 mm posts spaced on 11.7 mm centers. The area of the top of each post is 0.722 cm<sup>2</sup>, which is 55.4% of its 1.37 cm<sup>2</sup> cell. The root-mean-squared (also the arithmetic-mean) height-of-roughness is 3 mm.

The back surface of the plate has 9 precision electronic resistors embedded as heating elements and a temperature sensor. There is 2.54 cm thick thermal foam insulation between the back of the plate and a 0.32 mm thick sheet of aluminum. The aluminum sheet also has a temperature sensor at its center.

Figure 28 is a cross-section drawing of the plate assembly.

The Convection Machine wind-tunnel (Figure 29) has a 61 cm × 35.6 cm cross-section and a 61 cm depth. It allows the plate assembly to be centered with 15 cm of space on all sides. The fan pulling air

through the test chamber produces a maximum wind-speed of 4.5 m/s ( $Re \approx 9 \times 10^4$  for the 0.305 m square plate). Its minimum nonzero wind-speed is 0.12 m/s ( $Re \approx 2300$ ).

The 99% laminar and smooth-turbulent boundary-layer thicknesses for the wind-tunnel versus the distance  $x$  from its leading edge are:

$$\delta_{lam} = 4.92 \sqrt{\frac{x\nu}{V}} \quad \delta_{tur} = 0.37x^{4/5} \left(\frac{\nu}{V}\right)^{1/5}$$

Figure 30 shows that 150 mm clearance between the plate and wind-tunnel walls keeps the boundary layers from interacting at airspeeds within its range.

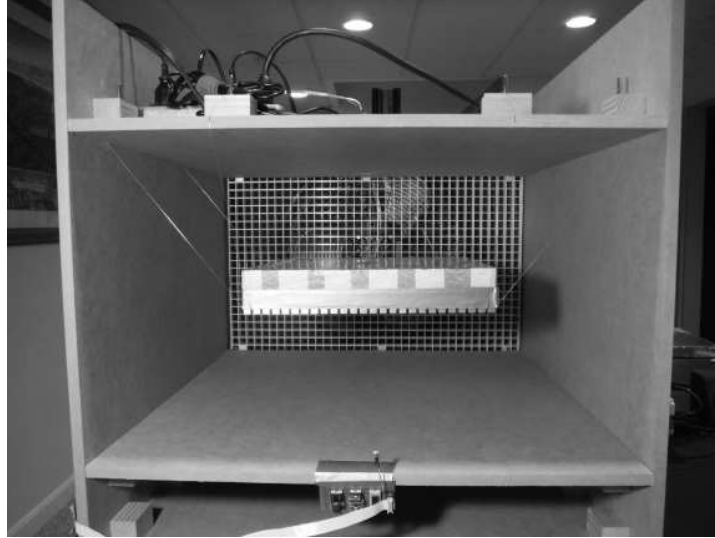


**Figure 29** 3 mm roughness plate in wind-tunnel

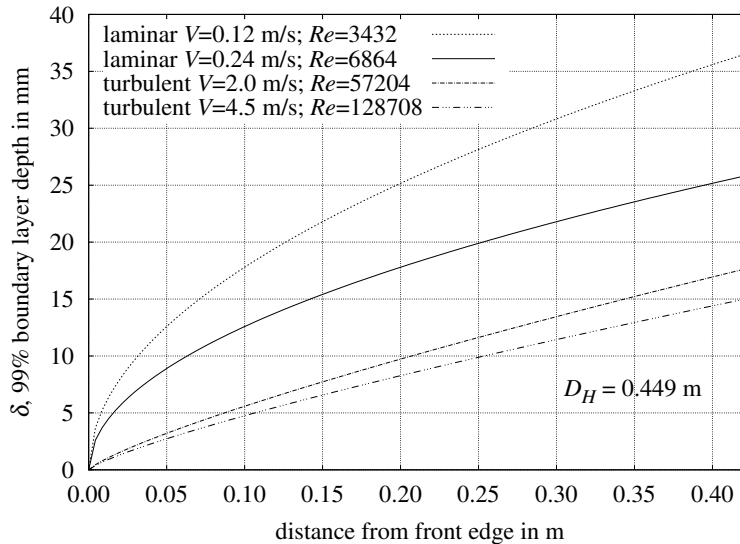


**Figure 30** wind-tunnel boundary layer thickness

The rotation rate of the fan is sensed by a photo-transistor receiving light from a LED being interrupted by the passing fan blades. Software controls a solid-state relay (supplying power to the fan) to maintain the fan rotation rate dialed into switches. At rotation rates less than 400 r/min, the software pulses power to the fan according to a phase comparator. At rates greater than 400 r/min it servos the duty cycle of a 10 Hz square-wave supplying power. It operates over a range of 32 to 1500 r/min.

The correspondence between fan rotations per second and wind-speed was made using an anemometer. The ABM-200 Airflow & Environmental Meter specifies an accuracy of  $\pm 0.5\%$  of reading from 2.2 m/s to 62.5 m/s. Figure 31 shows the calibration curve for the empty wind-tunnel.

For any fan, there must be some rotation rate and wind-speed  $V_s$  beyond which airflow doesn't increase. That flattening will appear gradually from slower rotation rates. Modeling the stall speed as  $V_s = 7.5$  m/s, equation (75) is the solid line in Figure 31. From 500 r/min to 1500 r/min, it matches measurements with a standard deviation of 0.0075 m/s.

$$V = [(rS)^{-2} + V_s^{-2}]^{-1/2} \quad (75)$$

$$S = \frac{V_{1500}}{1500 \text{ r/min} \sqrt{1 - (V_{1500}/V_s)^2}} \quad V_{1500} \approx 4.172 \text{ m/s}$$

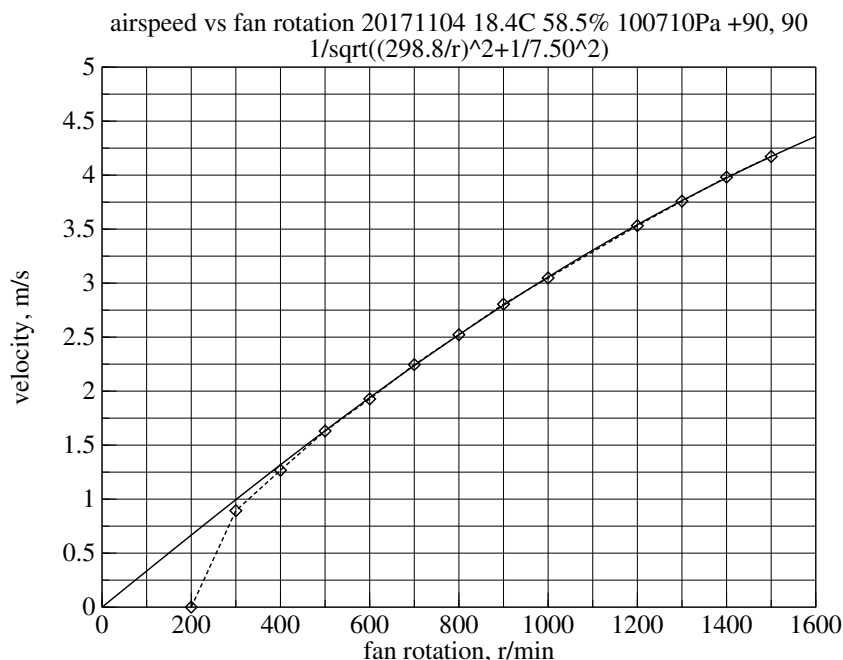


**Figure 31** airspeed vs fan rotation

The plate assembly is suspended from six lengths of 0.38 mm-diameter steel piano wire terminated at twelve zither tuning pins in wooden blocks around the test chamber. The wire is sheathed by 0.95 mm Teflon tubing where it would otherwise contact the plate metal.

With the plate assembly in the wind-tunnel, the airspeed is increased in proportion to the reduction of wind-tunnel aperture by the plate's cross-sectional area  $A_x$ :

$$V_p = V \frac{A_{wt}}{A_{wt} - A_x} \quad (76)$$

The calculated increase is 7.7% for the 3 mm roughness plate and 7.3% for the 1 mm roughness plate.

The ambient sensor board can be seen at the lower edge of the tunnel in Figure 29. This small board measures the pressure, humidity, and temperature of the air at the wind-tunnel intake. The LM35 temperature sensor projects into the wind-tunnel test chamber; it is wrapped in aluminum tape so that radiative heat transfer is minimized. The temperature sensor is powered only while it is being read so that self-heating doesn't affect it; self-heating was a problem before it was switched.

Logging of the measurements is performed by a STMicroelectronics STM32F3 Discovery 32-Bit ARM M4 72MHz development board. The custom electronics board which the STM32F3 plugs into, contains power supplies, heater control and drive, and signal conditioning.

A program was written for the microprocessor which takes measurements and writes them to the microprocessor's non-volatile RAM, controls the heater, servos the fan speed, and (later) uploads captured data to a computer over a USB serial interface. Every second for 108 minutes the program calibrates and reads each on-chip 12 bit analog-to-digital converter 16 times and sums its readings to create a 16 bit value.

Previous laboratory measurements [5] of forced convection have been performed by starting the fluid flow and plate heater, waiting for the system to reach equilibrium (as indicated by a stable plate temperature), then recording the measurements of the physical quantities.

Electronic sensors and digital processing make possible an entirely different measurement methodology. Rather than waiting for the plate to reach equilibrium before each measurement, the plate is preheated, then the state of all sensors is captured every second for 108 minutes as the plate is cooled by convection. The convection measurement is computed from the slope of plate temperature versus time.

The physical parameters from measurements and material specifications of both plate versions are:

$\varepsilon$	3 mm	1 mm	RMS height-of-roughness
$A$	0.093 m <sup>2</sup>	0.093 m <sup>2</sup>	plate test area
$C$	4690 J/K	4242 J/K	plate thermal capacity
$C_{bk}$	146 J/K	146 J/K	back thermal capacity
$U_I$	0.075 W/K	0.075 W/K	insulation thermal conductance
$\epsilon_p$	0.04	0.04	plate surface emissivity
$\epsilon_{wt}$	0.90	0.90	wind-tunnel test chamber emissivity

**Table 6 physical parameters**

The effective wind-tunnel emissivity  $\epsilon_{wt}$  may differ from the emissivity of medium-density-fiberboard (0.90 [26]) because the temperatures of the (internal) wind-tunnel surfaces may not be uniform, and the plate exchanges thermal radiation with objects in the room which may have different emissivities and temperatures than the wind-tunnel and air.

MIC-6 aluminum was chosen for its low emissivity ( $\epsilon_p = 0.04$ ); the radiative heat loss from the rough face of the plate is only 20 mW/K, about 2% of the 1.08 W/K expected for  $V = 1\text{m/s}$  convection.

The measured dynamic physical quantities are:

$V$	m/s	air velocity (from fan rotation rate)
$T_P$	K	plate temperature
$T_F$	K	air temperature
$T_B$	K	back surface temperature
$P$	Pa	atmospheric pressure
$\Phi$	Pa/Pa	air relative humidity

**Table 7 dynamic quantities**

At low flow rates, the sides of the insulation on the back of the test plate can leak more heat than the rough surface. The side heat transfers are simulated in order to discount them from the total heat flow. The calculated and simulated quantities are:

$U_S(V)$	W/K	side thermal conductance
$h_R$	W/(m <sup>2</sup> K)	radiative surface conductance
$\bar{h}(V, t)$	W/(m <sup>2</sup> K)	convective surface conductance
$T_P(V, t)$	K	plate surface temperature

**Table 8 calculated and simulated quantities**

$U_S(V)$  is the quantity of radiative emissions and natural convection from the sides reducing the net convection from the test surface.

Collecting terms which have a factor of  $T_P - T_F$  into  $U_T(V)$ , the heat balance equation for the plate during convection is:

$$U_T(V) = U_S(V) + \bar{h}(V) A + \epsilon_p \epsilon_{wt} h_R A \quad (77)$$

$$0 = U_T(V) [T_P - T_F] + U_I [T_P - T_B] + C \frac{dT_P}{dt} \quad (78)$$

Taken as functions of time  $t$ , include the 110 s delay for heat propagation through the insulation:

$$T_P(t) = \frac{U_T(V) T_F(t) + U_I T_B(t - 110) - C dT_P(t)/dt}{U_T(V) + U_I} \quad (79)$$

In order to compute Nusselt number  $\bar{Nu} = \bar{h} L/k$ , equation (79) is solved for  $\bar{h}(V, t)A$  from equation (77).

$$\eta(V, t) = -U_I [T_P(t) - T_B(t - 110)] \quad (80)$$

$$\bar{h}(V, t) A = \frac{\eta(V, t) - C [T_P(t) - T_P(t')]/[t - t']}{T_P(t) - T_F(t)} - A \epsilon_p \epsilon_{wt} h_R - U_S(V) \quad (81)$$

In the denominator of equation (81),  $\overline{T_P}(t)$  and  $\overline{T_F}(t)$  are the 11-element cosine averages of plate and fluid temperature (centered at time  $t$ ). Averaging is needed so that the derivative doesn't correlate with the denominator, causing bias.

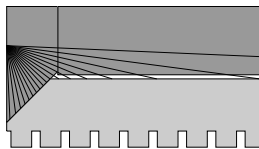


**Figure 32** conduction through XPS wedge

The four sides aren't isothermal surfaces; each has a 3.5 mm metal strip exposed running the length of the side with a wedge of extruded polystyrene foam (XPS) insulation filling the 16 mm bevel. Each point's effective surface conductance will depend on the temperature profile along the side.

A point on the side which is near to metal will have a large conductance. Summing the conductivity divided by the shortest distance to metal at each angle will be roughly proportional to the local conductance (see Figure 32). The conductance through a slab with parallel isothermal faces is  $k A/d$ . The ratio of the slab conductance to the slab sum is 0.637, which is used to normalize the calculated conductivities.

In forced air the four sides have three distinct behaviors. The forced air flows parallel to the long dimension on two sides but flows into the windward side and away from the leeward side. The windward and leeward sides don't contribute forced convection in the computation.

The smooth turbulent forced convective component for the two parallel sides  $U_{fi}(V)$  is computed by averaging the local forced convective surface conductance in series with the insulation thermal conductance over the area of the sides. Laminar flow isn't modeled; the lower bound of integration is  $Re_0 = 450$ . The expected convection through the two parallel sides is 9% of the convection from the 3 mm rough surface at 4 m/s wind-speed. Even a 10% error in the side convection predictions will affect the rough plate measurement by less than 1%.

symbol	nominal	sensitivity	bias	uncertainty	component
$T$	19.5K	-0.182%/K	1.0K	0.18%	LM35C temperature sensor
$\Delta T$	10.5K	8.371%/K	0.15K	1.26%	LM35C differential
$P$	101kPa	0.001%/Pa	1.5kPa	1.11%	MPXH6115A6U air pressure
$V$	2.00m/s	36.816%/m/s	20mm/s	0.74%	airspeed
$D_{Al}$	19.4mm	305.821%/m	500um	0.15%	slab thickness
$L_T$	8.50mm	-395.106%/m	500um	0.20%	block length
$\epsilon_{pv}$	6.00mm	5332.117%/m	200um	1.07%	P2V height-of-roughness
$L_m$	3.50mm	418.327%/m	500um	0.21%	side metal strip width
$C_{Pt}$	4.69kJ/K	0.019%/K	42J/K	0.78%	plate thermal capacity
$\epsilon_p$	0.040	15.075%	0.01	0.15%	plate emissivity
$\epsilon_{wt}$	0.900	6.198%	0.05	0.31%	wind-tunnel emissivity
$\theta$	90.0°	-0.155%/°	1.0°	0.15%	plate angle
				2.34%	combined bias uncertainty
symbol	nominal	sensitivity	variability	uncertainty	component
$\Delta T$	10.5K	8.371%/K	42mK	0.35%	temperature differential
$V$	2.00m/s	36.816%/m/s	7.5mm/s	0.28%	airspeed
				2.50%	RSS combined uncertainty

**Table 9** uncertainties for bi-level 3mm roughness at  $Re = 40860$

The last steps in processing a 108 minute measurement run are to calculate the sensitivities of the measured heat flow to each parameter at its mean value over the measurement interval, multiply each sensitivity by its estimated parameter bias to yield the component uncertainties, and then to calculate the root-sum-squared (RSS) of these uncertainties to yield the RSS measurement uncertainty as specified in Abernethy, Benedict, and Dowdell [27].

For the 3 mm roughness plate, Table 9 lists the sensitivity, bias, and uncertainty for each component contributing more than 0.15% uncertainty. The RSS combined measurement uncertainty is  $\approx 2.5\%$ .